

https://dspace.org/

The harmony search optimisation method as applied to high dose rate brachytherapy

Mason, Lara

2019
https://hdl.handle.net/10539/27067

Downloaded from a DSpace repository. https://dspace.org/

UNIVERSITY OF THE WITWATERSRAND

RESEARCH REPORT

The Harmony Search optimisation method as applied to high dose rate brachytherapy

---

Author:
Lara MASON

Supervisor:
Prof. James LARKIN

A research report submitted to the Faculty of Science, University of the Witwatersrand, Johannesburg, in partial fulfilment of the requirements for the degree of Master of Science

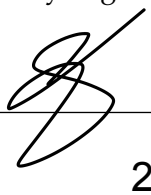
in the

Department of Physics

January 23, 2019

Declaration of Authorship

I, Lara MASON, declare that this research report titled, "The Harmony Search optimisation method as applied to high dose rate brachytherapy" is my own, unaided work. It is being submitted for the Degree of Master of Science at the University of the Witwatersrand, Johannesburg. It has not been submitted before for any degree or examination at any other university.

Signed: 

Date: 23 January 2019

University of the Witwatersrand

Abstract

Faculty of Science
Department of Physics

Master of Science

The Harmony Search optimisation method as applied to high dose rate brachytherapy

by Lara MASON

This research report presents an investigation into the dose calculation used for planning of high dose rate brachytherapy treatment for cervical cancer using Monte Carlo methods, including the implementation of a novel optimisation algorithm, the Harmony Search method. The optimisation is implemented using the Geant4 Monte Carlo simulation toolkit. Monte Carlo methods are also applied to the investigation of the AAPM TG-43 parameters, which define the dose calculation formalism used in high dose rate brachytherapy treatment planning. The parameters of the AAPM TG-43 protocol are calculated and compared to data. The Harmony Search algorithm is successfully implemented in optimising a brachytherapy treatment plan, and produces an optimal solution which fits the constraints imposed on it. The algorithm shows promise in future application to brachytherapy for cervical cancer treatment planning.

Acknowledgements

The first word of thanks must go to my supervisor, Prof. Larkin. Thank you for your support, for being a calming voice, and of course for bringing your dogs to the office sometimes. I'm not sure where I'd be if you hadn't stepped in at the beginning of the year, so thank you. Thanks also to Sonwabile, for all your help with Monte Carlo - thank you for showing me how to make Geant4 actually do something, and for everything from that point onwards. I appreciate your time and wisdom so much. Thanks too to Prof. Keartland, for his guidance and extensive help on the administration side.

A huge thank you and a note of admiration is paid to the Geant4 team for their very useful examples and extensive documentation, as well as patient responses to pleas for help. Geant4 is a wonderful toolkit, and I appreciate the opportunity to use and learn from it.

Of course, thanks as always to my family and friends, to Sean for his unwavering confidence in me, and to my Dad, whose unconditional love and support has got me to where I am today.

Contents

Declaration of Authorship **ii**

Acknowledgements **iv**

1 Introduction **1**

2 Dosimetry **4**
2.1 Ionizing Radiation . . . 4
2.1.1 Ionizing Photon Radiation . . . 5
2.1.2 Ionizing Particulate Radiation . . . 5
2.2 Sources of Radiation . . . 6
2.2.1 β^- Decay . . . 8
2.2.2 Electron Capture . . . 8
2.3 Interaction of Radiation with Matter . . . 8
2.3.1 Interaction of Photons with Matter . . . 9
2.3.1.1 Rayleigh Scattering . . . 10
2.3.1.2 Compton Scattering . . . 10
2.3.1.3 The Photoelectric Effect . . . 11
2.3.1.4 Pair and Triplet Production . . . 11
2.3.2 Interaction of Charged Particles with Matter . . . 11
2.4 Dose . . . 12
2.4.1 Radiation Field . . . 13
2.4.2 Indirectly Ionizing Radiation . . . 13
2.4.3 Directly Ionizing Radiation . . . 14

3 Brachytherapy **16**
3.1 Radiobiology . . . 16
3.2 Brachytherapy for Cervical Cancer . . . 17
3.3 Intracavitary Brachytherapy . . . 19
3.3.1 Afterloading Technology . . . 19

4 Treatment Planning and Reporting Standards **21**
4.1 Dose Calculation using AAPM TG-43 . . . 21
4.1.1 Two-Dimensional Dose Rate Formalism . . . 22
4.1.2 Simplifying Assumptions . . . 24
4.2 Recording and Reporting . . . 25

5 Monte Carlo simulation using Geant4 **27**
5.1 Geant4 . . . 27
5.1.1 Particle Transport . . . 28
5.1.2 Particle Interactions . . . 28
5.2 Gammamed Source Simulation . . . 29
5.2.1 Source Energy Spectrum . . . 31
5.2.2 Comparison to Reference Data . . . 31
5.2.3 Source Calibration . . . 33
5.2.3.1 Calibration Theory . . . 34
5.2.3.2 Calibration Set-Up . . . 34
5.2.3.3 Calculation of Kerma for Calibration . . . 34
5.2.3.4 Calibration Results . . . 36
5.3 AAPM TG-43 Parameters . . . 37
5.3.1 Geometry Function $G_L(r,\theta)$ . . . 37
5.3.2 Anisotropy Function $F_L(r,\theta)$ . . . 38
5.3.3 Radial Dose Function $g_L(r)$ . . . 43
5.4 Uncertainty . . . 43
5.4.1 Counting Statistics . . . 43
5.4.2 Uncertainty on AAPM TG-43 parameters . . . 44

6 Optimisation using the Harmony Search Algorithm **46**
6.1 Optimisation . . . 46
6.1.1 Harmony Search Theory . . . 47
6.1.2 The Objective Function . . . 50
6.2 Implementation of the Harmony Search . . . 50
6.2.1 Applicators . . . 51
6.2.2 Optimisation specifics . . . 51
6.2.3 Optimisation results . . . 54

7 Application to Future Research **57**

8 Conclusion **58**

List of Figures

2.1 The decay scheme of ^{192}Ir, showing both electron capture and β decay modes [13]. 7
2.2 The dependence of the dominant photon interaction mechanisms on energy, E and atomic number, Z [9]. 10

3.1 Computer-simulated tracks of 1 keV electrons showing the size of the clusters in relation to the size of the DNA [14]. 17
3.2 Creation of free radicals, $R*$, in nearby water molecules, termed indirect action, or within the DNA molecule, termed direct action [14]. 18
3.3 Intracavitary brachytherapy applicator employing a tandem and ring system [20]. 20

4.1 The two-dimensional coordinate system used by AAPM TG-43 in order to calculate the dose at point $P(r, \theta)$ [4]. 23
4.2 Recommended absorbed dose calculation points for critical structures. 25

5.1 Materials and dimensions (mm) of the GammaMed source [32]. 29
5.2 Simulation of the GammaMed ^{192}Ir source in air where the iridum core and capsule details are visible. 30
5.3 Energy spectrum of primary particles from the GammaMed source simulated in this report. 31
5.4 A depiction of the source undergoing decay events within the water phantom, denoted as a blue cube, used for the dose rate comparison to reference data. 32
5.5 Normalised radial dose comparison between simulation using Geant4 and published reference data. 33
5.6 The geometry used for the calibration process is shown, with 5 decay events simulated. . . 35
5.7 An example of the assignment of tracks moving through a volume. 36
5.8 The geometry relevant to the determination of β, where the source length is $|SF|$, the measurement point is P, and the line $|MP$ joining the source centre to the measurement point has length r. 37
5.9 Values of $r^2 G_L(r, \theta)/G_L(r_0, \theta_0)$ for $\theta = 0°, 10°, 20°, 30°, 40°$, and $50°$. 39
5.10 Values of $r^2 G_L(r, \theta)/G_L(r_0, \theta_0)$ for $\theta = 60°, 70°, 80°$, and $90°$. 40
5.11 Values of $F_L(r, \theta)$ for $\theta = 0°, 10°, 20°, 30°, 40°$, and $50°$. 41
5.12 Values of $r^2 G_L(r, \theta)/G_L(r_0, \theta_0)$ for $\theta = 60°, 70°, 80°$, and $90°$. 42
5.13 The radial dose function $g_L(r)$ plotted against reference data. 43

6.1 Diagram of a tandem and ring applicator as simulated in this report [20]. 51
6.2 Tandem and ring applicator as simulated using Geant4. The dwell points for the optimisation are numbered 1-11. 52

List of Tables

2.1 Allowed decay modes of ^{192}Ir and their associated γ emission energy. 7

6.1 Constraints set for the optimisation. 53
6.2 Harmony Memory vectors at the initialisation of the simulation. 55
6.3 Vectors initialised during the iterations. 55
6.4 Vectors initialised during the iterations (continued). 56
6.5 Harmony Memory vectors at the conclusion of the simulation. 56

Chapter 1

Introduction

Curative treatment for cervical cancer necessitates the use of external beam radiation therapy combined with interstitial or intracavitary brachytherapy. Brachytherapy is a type of radiation therapy in which a radioactive source is placed in close proximity to the tumour or region to be treated. The use of brachytherapy in the treatment of cervical cancer is strongly recommended in the literature, and significantly better survival rates are seen when patients are treated with a combination of both radiation therapy modalities [1]. This is due to the fact that brachytherapy alone can deliver a highly effective dose to the tumour volume, while providing a greater sparing to the surrounding organs at risk than could be achieved using external beam radiotherapy alone.

The goal of radiotherapy is to deliver a sufficient dose to the target, as well as to reduce or avoid side effects by limiting the radiation dose delivered to surrounding normal tissues. In order to ensure this is achieved, the radiation dose to the organs and structures of interest should be calculated [2]. This is achieved through treatment planning. In recent years, there have been significant advances made in the field of brachytherapy for cervical cancer. Radiation therapy treatment planning has moved from conventional x-ray-based planning to three-dimensional planning, with the incorporation of imaging modalities such as computed tomography (CT) into the planning programme allowing for direct visualisation of targets and critical organs [3]. While some treatment centres are moving towards fully Monte Carlo-based treatment planning, lower resource centres, defined as those with higher volumes of patients and fewer financial resources, rely on semi-generalised treatment planning for brachytherapy. In this report, the treatment planning system used by one such centre, Charlotte Maxeke Johannesburg Academic Hospital (CMJAH), has been investigated through the use of a Monte Carlo simulation, and an optimisation has been performed on a simulated standard brachytherapy treatment using the Harmony Search optimisation algorithm, which is not currently used at a clinical level. This is done in order to assess whether this optimisation algorithm has the potential to be implemented in such a clinical centre.

The nature of the brachytherapy treatment for cervical cancer of interest to this report is a radioactive source moving through hollow applicators which are inserted intravaginally. The movement of the source through the applicators is customisable, and a mathematical optimisation algorithm may be used to achieve the best possible treatment. The brachytherapy treatments for cervical cancer at CMJAH are carried out using an ^{192}Ir source, and planned using the American Association of Physicists in Medicine Task Group Number 43 (AAPM TG-43) protocol [4], which describes how to calculate the dose to a point, due to radiation emitted by a source at some distance away. The protocol describes a two-dimensional dose calculation formalism, which estimates the dose rate at a point based on some pre-calculated factors related to the source, approximating the body as a cylinder of water. The AAPM TG-43 protocol is

clinically implemented through the use of a computerised radiotherapy treatment planning system, where the dose distribution is mapped onto a two-dimensional CT scan of the patient. A CT scan is created using cross-sectional x-ray images of the patient, which are compiled to make a three-dimensional image, allowing for a three-dimensional visualisation of the dose distribution. The planning system then performs an optimisation on the positioning of the brachytherapy source to achieve the most efficient treatment. Medical physics plays a significant role in the use of radiation sources in a radiation oncology programme, including the development of treatment plans according to these protocols, verifying the calibration of the brachytherapy sources, and the calculation of dose distributions.

An alternative to the two-dimensional dose calculation-based treatment planning described by the AAPM TG-43 protocol is the use of Monte Carlo-based planning, where a simulation is used to measure the dose from first principles, that is, by measuring the dose directly from the deposition of energy to a volume. This is an alternative to using a dose calculation formalism to estimate the dose due to a given source at some distance. The use of Monte Carlo techniques in fields such as radiation dosimetry, radiotherapy physics, and radiation physics has vastly increased in recent years due to the significant increase in speed of simulation techniques and the decrease in cost of data-processing that has occurred [5]. Further to this, general computing power has increased, and continues to increase, dramatically. General-purpose Monte Carlo software packages have become available to the common user. Given the use of high-energy electron and photon beams and sources which are being used for radiotherapy, the understanding and correct simulation of electron transport and interactions for dosimetry and treatment planning purposes are becoming more crucial, which can only be handled completely generally through the use of Monte Carlo simulations. [5].

In this report, a Monte Carlo simulation has been done using one such software package, Geant4 [6], a general purpose toolkit written in C++ which includes a set of physics models which are of use to medical physics simulations, in order to investigate a new optimisation method, the Harmony Search algorithm, which may be used for Monte Carlo-based treatment planning. An examination of the available literature does not show an application of this algorithm to brachytherapy for cervical cancer treatment yet, so this application has been examined in this report. A simulation-based optimisation using the Harmony Search algorithm has been done on a simplified brachytherapy treatment plan, using a Monte Carlo-based estimation of the dose distribution. It is an algorithm based on inverse planning, where the desired dose distribution, characteristed using constraints, is defined prior to the optimisation beginning. This process needs no manual adjustment, unlike conventional methods [7]. Inverse planning has been growing in popularity over the last decade; the use of constraints ensure that the objectives of the physicist are realised, and there is no need for any manual adjustment or human bias. As there is a move towards Monte Carlo-based treatment planning systems at better resourced centres, it is instructive to examine an application of this using the Harmony Search optimisation method.

In simulating a brachytherapy source on which to perform the optimisation, the dose calculation formalism given by the AAPM TG-43 protocol currently used at CMJAH has also been examined. In order to achieve this, the simulation has been used to verify the AAPM TG-43 parameters used in the dose calculation formalism. This work has been done in order to assess the applicability of the Geant4

Monte Carlo toolkit to the brachytherapy context, as well as to investigate the AAPM TG-43 protocol which forms a vital part of the brachytherapy treatment planning at CMJAH, and at many other radiotherapy centres around the world.

Given that the basis of medical physics is the understanding and continuing development of dosimetry, a portion of the theory at the beginning of this paper is dedicated to the key concepts of current dosimetry in radiation therapy. Critical concepts from the dosimetry section will also be carried into the Monte Carlo simulation in the later portion of this report.

In Chapter 2, a description of the field of dosimetry and the concept of dose is given. An overview of the theory of radiation used for radiotherapy will be given, including sources of radiation in Section 2.2 and the interaction of radiation with matter in Section 2.3. Following this, Section 2.4 provides a description of the dose to a given medium due to ionizing radiation, and outlines important quantities related to dose which are used in dosimetry theory. Chapter 3 describes the theory of brachytherapy as it pertains to this report, including the ideas of radiobiology which allow for the use of radiation in cancer therapy in Section 3.1. Section 3.2 will discuss the theory of brachytherapy, and Section 3.3 will discuss intracavitary brachytherapy as is used for the treatment of cervical cancer, as well as the equipment at CMJAH used for this purpose. Chapter 4 outlines the treatment planning and reporting protocols used at CMJAH, including the AAPM TG-43 dose calculation formalism which is to be investigated in this report, and a discussion of the designation of points to represent target organs.

Following these chapters on the theory of the report, Chapter 5 describes the Monte Carlo method and Geant4 simulation package, including a description of the reconstructed radioactive source in Section 5.2, and the verification of the AAPM TG-43 planning parameters in Section 5.3. In Section 5.4, the uncertainties relevant to this report are discussed. In Chapter 6, the optimisation method is detailed, including a description of optimisation techniques in Section 6.1 and, in particular, the Harmony Search algorithm theory in Section 6.1.1. The theory underlying objective functions is discussed in Section 6.1.2. Following this, the implementation of the Harmony Search algorithm in this report is described in Section 6.2, including a description of the simulation geometry in Section 6.2.1, the specifics of the optimisation in Section 6.2.2, and the results in Section 6.2.3. In Chapter 7, an outlook on further research is given. Finally, Chapter 8 offers a discussion of the results, including their applicability to current and future clinical protocol.

Chapter 2

Dosimetry

Radiation is the propagation through space of energy in an electromagnetic or particulate form. It may be emitted during nuclear decay, annihilation of matter and antimatter, atomic energy transitions, acceleration of charged particles, or particle-particle interactions. Radiation can be classified as ionizing or non-ionizing, where ionizing radiation deposits energy into the material through which it travels. This is because ionizing radiation is defined as being energetic enough to liberate (ionize) orbital electrons from atoms with which the radiation interacts. The energy transferred from the radiation to the electrons is sufficient to overcome their binding energy, which frees the electrons and causes ionisation of the atom.

The biological effect that ionizing radiation induces in a tissue is proportional to the amount of energy per unit mass deposited therein. This energy is quantified by the absorbed dose D, and is the integral characteristic of radiation oncology, as the dose deposition in a given tissue governs the treatment of the disease. The dose is defined [8], [9]

$$D = \frac{d\bar{\epsilon}}{dm}, \tag{2.1}$$

where dm is the mass of the volume element in question, to which energy $d\bar{\epsilon}$ is imparted. Absorbed dose is measured in Gray (Gy). The study of the dose deposited in a medium due to the energy imparted by ionizing radiation is called dosimetry. In the following section a description of the field of dosimetry is given. The theory is summarised from [8] and [9], unless otherwise stated. In order to quantify the absorbed dose in a material, we must first investigate the radiation fields present and their interaction with the material.

2.1 Ionizing Radiation

Energy may be deposited in a medium by ionizing radiation passing through it, which may cause changes to the structure of the atoms. Ionizing radiation may be charged or uncharged, particulate or electromagnetic; the only requirement is that it has sufficient energy to ionize the orbital electrons within the medium. As this report concerns a simulation of a brachytherapy treatment, we will consider ionizing radiation that can be introduced into the medium by nuclear decay, described in Section 2.2. This radiation may then go on to introduce further radiation into the medium by interactions with the nuclei or orbital electrons, described in Section 2.3.

2.1.1 Ionizing Photon Radiation

Ionizing photon radiation is classified into four distinct types; characteristic x-rays, gamma(γ)-rays, bremsstrahlung radiation, and annihilation quanta. The first usually results from atomic processes, the second from nuclear processes, the third from particle-atom and particle-particle interactions which cause deceleration of the incoming particle, and the fourth from electron-positron annihilation.

Characteristic radiation is produced when a bound orbital electron drops to a lower atomic energy state, known as an atomic energy transition. This occurs due to a vacancy left in one of the inner orbitals after an electron has been released due to ionization or atomic decay. The difference in energy between the initial higher energy state and final lower energy state may be released via the emission of a fluorescence x-ray, termed a characteristic x-ray. γ-rays are photons which are produced as a result of transitions between nuclear energy levels. Bremsstrahlung radiation is produced when a charged particle is accelerated or decelerated upon interaction with an electromagnetic field, such as the Coulomb field of a nucleus. Annihilation quanta, two back-to-back photons most commonly with energies of 511 keV each, result from the annihilation of a positron with a free and relatively stationary electron [9].

Ionizing photon radiation is termed indirectly ionizing radiation, as photons transfer energy to charged particles within the medium via interactions such as the photoelectric effect, which then go on to cause secondary ionizations within the medium via direct reactions [10]. These secondary ionizing particles can go on to cause a cascade of ionization events.

2.1.2 Ionizing Particulate Radiation

Ionizing particulate radiation is most commonly electrons and positrons, which can be produced in a variety of ways and are given names accordingly. They are defined to be directly ionizing radiation, as they transfer energy to the medium via direct Coulomb interactions which result in energy deposition. Types of electrons include Auger electrons, beta(β)-particles, internal conversion electrons, and δ-rays.

Auger electrons are emitted via a process which competes with the emission of characteristic radiation. As in the emission of characteristic radiation, an electron from a higher energy orbital transitions to a lower energy state to fill a hole left by an electron which has left the shell. Rather than emit the difference in binding energies via a photon, the atom can eject an outer shell electron, termed an Auger electron, with an energy equal to the state transition energy difference less its own binding energy. Beta rays and internal conversion electrons result from nuclei decaying via β^- emission and internal conversion respectively. An electron which is directly ejected from an atom by ionizing radiation is called a δ-ray.

Positrons can be produced via pair production or triplet production during photon interactions with matter, as is described in Section 2.3.1. Positrons are also emitted by nuclei which decay via β^+ emission, and will then likely interact with an orbital electron to produce annihilation quanta.

2.2 Sources of Radiation

Ionizing radiation may be introduced into a medium due to nuclear processes such as radioactive decay, as will be discussed in this section, particle-particle or particle-atom interactions within the medium, as will be discussed in Section 2.3, or it may enter as an external beam of photons, electrons or other particulate radiation as used in external beam radiotherapy or diagnostic radiation, which will not be discussed. Radioactive decay may result in particulate (electrons and positrons) or electromagnetic (photons) radiation, or a combination of these.

Brachytherapy relies on the process of radioactive decay, by which radioactive sources of energetically unstable nuclei produce the radiation used for treatment. Radioactive decay refers to the spontaneous changes in the nucleus or orbital electrons of an unstable parent nuclide, or radionuclide, through which the nucleus loses energy and transforms to a lower energy state or to an entirely new daughter nuclide. A nuclide is an atom with a specified number of protons and neutrons in its nucleus. The energy is emitted in the form of radiation, which may be particulate or electromagnetic. A nuclide has a given activity A, defined in terms of a specific decay constant λ as [9]

$$A = \lambda N = -\frac{dN}{dt} \tag{2.2}$$

for N identical parent nuclides. Integration of Equation 2.2 describes the reduction in number of parent nuclides with time as

$$N_t = N_0 \exp^{-\lambda t}. \tag{2.3}$$

Equation 2.3 can then be used to obtain the half life, $t_{\frac{1}{2}}$, defined as the time required for the initial number of parent nuclides to halve, by substituting $N_t = \frac{N_0}{2}$. This yields

$$t_{\frac{1}{2}} = \frac{\ln 2}{\lambda}. \tag{2.4}$$

Should a radionuclide have more than one decay mode, as is common, the decay constant λ is expressed as the sum of the individual decay modes [9],

$$\lambda = \sum_i \lambda_i. \tag{2.5}$$

The mode of radioactive decay of a given nuclide is particular to its structure. The modes of decay most relevant to clinical dosimetry are α decay, β decay, electron capture, isomeric transformation (γ decay) and internal conversion, which emit ionizing photon and/or particulate radiation. The general equation for radioactive decay is written [9]

$${}^{A}_{Z}P \rightarrow {}^{A-A_R}_{Z-Z_R}D + {}^{A_R}_{Z_R}R + \sum Q, \tag{2.6}$$

where A is the atomic mass number defined as the number of protons and neutrons in the nucleus, Z is the atomic number, representing the number of protons in the nucleus, and in general [9]

$$\sum Q = M_P - M_D - M_R \tag{2.7}$$

γ energy (keV)	Probability (%)
β^- Transitions	
53.3	0.0033
258.7	5.59
538.8	41.4
675.1	47.9
Electron Capture Transitions	
136.6	0.095
355.8	3.97
465.9	0.686

TABLE 2.1: Allowed decay modes of ^{192}Ir and their associated γ emission energy.

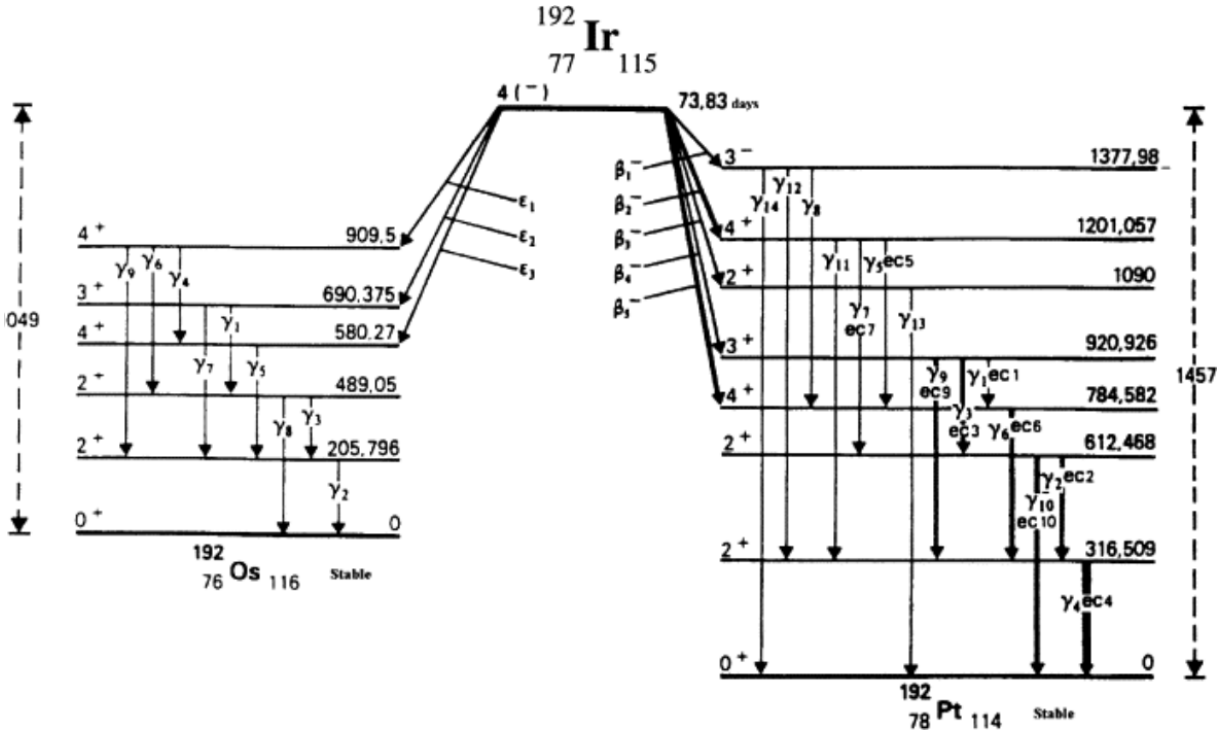


FIGURE 2.1: The decay scheme of ^{192}Ir, showing both electron capture and β decay modes [13].

is the total energy released by the disintegration process excluding the rest masses of the products.

In this report ^{192}Ir will be used as the radioactive source, as it is the most commonly used radionuclide in high dose rate (HDR) brachytherapy [11], and is used for the treatment of cervical cancer at CMJAH. ^{192}Ir has a half life of 73.827 days, decaying 95.13% of the time to an excited state of ^{192}Pt via β^- emission, and 4.87% of the time to an excited state of ^{192}Os via electron capture. The spectrum of γ released during these decay modes have a variety of energies, which are tabulated in Table 2.1 [12], and may be visualised using Figure 2.1. These decay modes are reproduced in the Monte Carlo simulation of the ^{192}Ir source, and are described in further detail below.

2.2.1 β^- Decay

β^- decay occurs when a neutron in a nucleus spontaneously converts to a proton and emits an electron (known as a β^-) and an antineutrino $\overline{\nu}$. The process is written [9]

$$ {}^{A}_{Z}P \rightarrow {}^{A}_{Z+1}\, D + \beta^- + \overline{\nu} + \sum Q, \tag{2.8} $$

where $\sum Q$ is shared between the kinetic energy of the β particle, the antineutrino, and the energy of any de-excitation photons. The beta decay specific to ^{192}Ir can then be written

$$ {}^{192}_{77}Ir \rightarrow {}^{192}_{78}\, Pt + \beta^- + \overline{\nu} + \sum Q. \tag{2.9} $$

2.2.2 Electron Capture

The less common mode of decay for ^{192}Ir is electron capture, where a nucleus captures an orbital electron and a proton converts to a neutron, emitting a neutrino in the process. The general formula is written [9]

$$ {}^{A}_{Z}P + e^- \rightarrow {}^{A}_{Z-1}\, D + \nu + \sum Q. \tag{2.10} $$

The energy $\sum Q$ is shared between the neutrino and any de-excitation photons. Since neutrinos and antineutrinos can only interact via the weak force, they are considered to be non-ionizing radiation. The electron capture decay mode specific to ^{192}Ir can then be written

$$ {}^{192}_{77}Ir + e^- \rightarrow {}^{192}_{76}\, Os + \nu + \sum Q. \tag{2.11} $$

2.3 Interaction of Radiation with Matter

As radiation traverses matter, it interacts with the orbital electrons and nuclei of the atoms. The interaction that occurs depends on the type and energy of the radiation, and can also depend on the binding energy of the orbital electron, the atomic number Z of the nucleus, and the distance at which the radiation interacts with the nucleus or electron [9]. Scattering collisions between the incoming radiation and the atomic nuclei or orbital electrons can be elastic, where total kinetic energy and momentum are conserved, or inelastic, where total kinetic energy can change due to radiative losses or atomic excitations. The path of the incoming radiation may be altered through scattering, and it may transfer energy to the medium (termed collisional losses) or to photons (termed radiative losses). Total momentum must always be conserved.

In order to simulate a brachytherapy treatment plan, all interactions between radiation, both electromagnetic and corpuscular, and the material must be considered and accounted for. This requires knowledge about the interactions and the probabilities with which they will occur. Photons and charged particles undergo very different interactions when traversing media, and these processes are individually considered within the Geant4 simulation. The types of indirectly ionizing radiation described in Section 2.2, although given different names and with different production modes, are all photons and so interact with matter in the same way, described in Section 2.3.1. The charged particle interactions described in Section 2.3.2 are those pertaining to electrons and positrons, as those are the

charged particles relevant in this work. The interactions of radiation with the medium defines the dose that is deposited therein.

2.3.1 Interaction of Photons with Matter

Photon interactions with the atoms of a given material take place with a probability dependent on the energy of the photon and the atomic number Z of the material. A tightly bound orbital electron is defined to have a binding energy on the order of the photon's energy. The binding energy of a free electron is defined as having a much lower energy than that of the photon. The photon may also interact with the field of the nucleus. During an interaction the photon may be scattered or may disappear completely. The dominant interaction processes are Compton scattering, Rayleigh scattering, the photoelectric effect, pair production, and triplet production. These processes are all considered in the Monte Carlo simulation using Geant4.

Given a beam of particles passing through some absorber material, the attenuation coefficient μ is defined in order to describe the removal of primary particles from the beam. We can then write the total attenuation coefficient for a given photon beam as [9]

$$\mu = \sigma_R + \sigma_{CS} + \tau + \kappa + \eta, \tag{2.12}$$

where σ_R is the attenuation coefficient of Rayleigh scattering, σ_{CS} is the attenuation coefficient of Compton scattering, τ is the attenuation coefficient of the photoelectric effect, κ is the attenuation coefficient of pair production and η is the attenuation coefficient of photonuclear interactions. The dominant effects that a photon beam will undergo are displayed in Figure 2.2. When an ^{192}Ir source undergoes atomic decay, photons with energies ranging from 0.05 MeV to approximately 0.7 MeV are produced [12]. When a source is placed in water (Z=10) or a water-equivalent material, it is clear from Figure 2.2 that the dominant effect over the energy range of the photons produced by the decay of ^{192}Ir will be Compton scattering.

This attenuation depends not only on the particle type and energy but also on the density of the material in question, so we define the mass attenuation coefficient, μ/ρ, in order to remove the density dependence. In describing the interaction of photons with matter, we further define the mass-energy transfer coefficient μ_{tr}/ρ. This is a quantity of interest since electromagnetic radiation ionizes matter by first transferring energy to secondary electrons via one of several interaction processes. μ_{tr}/ρ is proportional to the average energy transferred to the medium, $\overline{\epsilon_{tr}}$. In order to simulate energy deposited in a medium by ionizing photon radiation, the mass-energy transfer coefficient must be known in order to quantify the energy transferred to the secondary electrons.

The mass energy transfer coefficient is defined [9]

$$\frac{\mu_{tr}}{\rho} = \left(\frac{\overline{\epsilon_{tr}}}{h\nu}\right)\frac{\mu}{\rho}. \tag{2.13}$$

The mass-energy transfer coefficient is then critical to calculating the dose deposited in a medium by ionizing photon radiation.

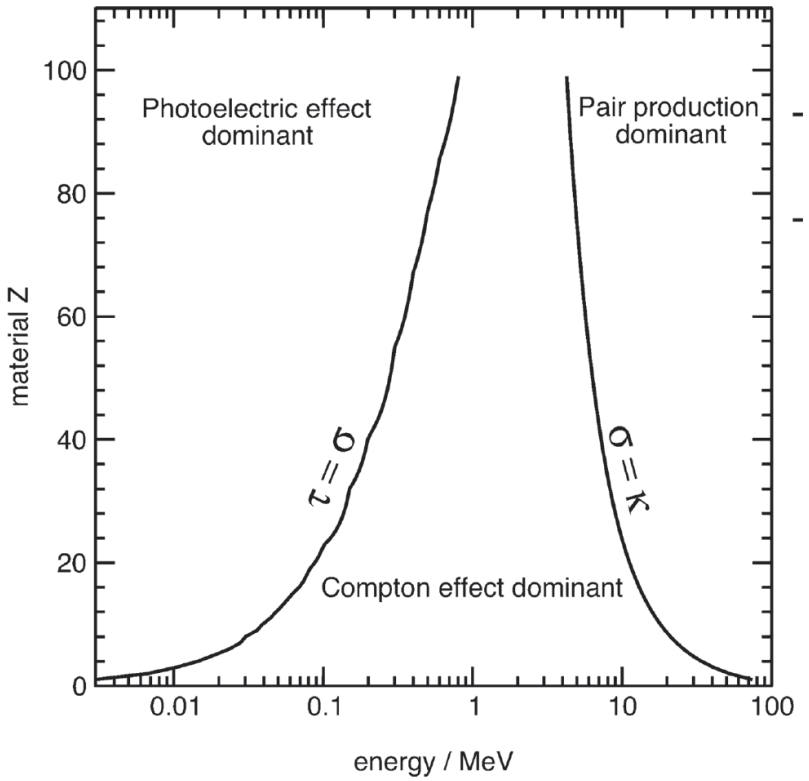


FIGURE 2.2: The dependence of the dominant photon interaction mechanisms on energy, E and atomic number, Z [9].

2.3.1.1 Rayleigh Scattering

Rayleigh scattering, or coherent scattering, occurs when a photon scatters off an entire atom. This takes place primarily at low photon energies, where the energy of the incoming photon is much less than the rest mass of the orbital electron. The scattering is elastic, meaning that the photon loses a negligible amount of energy [9]. This implies that a negligible amount of energy is transferred to the medium, and so this process contributes very little to the dose deposited in the medium.

2.3.1.2 Compton Scattering

Compton scattering occurs when an incident photon with energy $h\nu$ interacts with and transfers some energy to an oribital electron which is essentially free and stationary. The electron is ejected from the atom, and the photon is scattered. Compton scattering results in an electron vacancy in an inner orbital which can result in characteristic x-rays and Auger electrons. As the energy of these secondary particles is small compared to that of the scattered electron and photon, they are often ignored in non-Monte Carlo dosimetric applications [9]. However, in this paper, we are able to consider them using a Monte Carlo simulation.

Defining $\overline{T_0}$ as the mean initial kinetic energy of the ejected electron, the mass energy transfer coefficient is given by multiplying the fraction of the initial photon energy which is transferred to the electron by the mass attenuation coefficient [9],

$$\frac{\sigma_{CS,tr}}{\rho} = \frac{\overline{T_0}}{h\nu}\frac{\sigma_{CS}}{\rho}. \tag{2.14}$$

2.3.1.3 The Photoelectric Effect

The photoelectric effect occurs when a photon of energy $h\nu$ interacts with a tightly bound orbital electron of binding energy E_b. The photon transfers the entirety of its energy to the orbital electron, which is ejected from the atom, and the photon disappears. The electron escapes the orbital with some kinetic energy $T_{e^-} = h\nu - E_b$ [9] at an angle θ to the incident photon's direction. The recoil of the atom is negligible.

The orbital vacancy left by the ejection of the electron may again be filled via emissions of characteristic x-rays or Auger electrons. In the case of the photoelectric effect, the ejected electron and the Auger electrons contribute to the energy transfer considered by the mass energy transfer coefficient. Should all of the emissions to fill the lower energy state be Auger electrons, the sum of their kinetic energies will be the initial binding energy E_b [9]. Should some emissions take the form of characteristic x-rays, the energy transferred to secondary electrons, T, will be diminished. The mass energy transfer coefficient is then [9]

$$\frac{\tau_{tr}}{\rho} = \frac{\tau}{\rho}\frac{\overline{T}}{h\nu}, \qquad \overline{T} = h\nu - h\overline{\nu}_{x-rays}, \tag{2.15}$$

where $h\overline{\nu}_{x-rays}$ is the mean energy transferred to the characteristic x-rays.

2.3.1.4 Pair and Triplet Production

Pair production occurs when a photon interacts with the Coulomb field of a nucleus and creates an electron-positron pair. The threshold energy of the photon is $2m_ec^2$ which is the rest mass of an e^+e^- pair. Any additional energy is then transferred to the e^+e^- pair as kinetic energy. Momentum conservation requires that the photon be within the field of a nucleus when pair production occurs. This is due to the fact, in the electron-positron rest frame, the momentum of the initial photon with energy $E \geq 2m_ec^2$ must be cancelled out by the recoil of the nucleus. The total kinetic energy transferred to the electron positron pair is [9]

$$\overline{T} = h\nu - 2m_ec^2. \tag{2.16}$$

Triplet production is a similar process to pair production, but it occurs within the Coulomb field of an orbital electron which is then ejected. Since pair and triplet production have the same kinetic energy available to charged particles, their mass-energy transfer coefficients are the same. The fraction of energy transferred to charged particles is [9]

$$T_{avail}/h\nu = (h\nu - 2m_ec^2)/h\nu \tag{2.17}$$

and so the mass energy transfer coefficient is then defined as [9]

$$\frac{\kappa_{tr}}{\rho} = \frac{\kappa}{\rho}\left(\frac{h\nu - 2m_ec^2}{h\nu}\right). \tag{2.18}$$

2.3.2 Interaction of Charged Particles with Matter

As charged particles are the agents of energy deposition in matter, a good understanding of their interaction with materials is vital to accurate dosimetry studies. In order to model the dose distribution in a given material due to any type of ionizing radiation, the interactions of the secondary particles must

be known and well modelled. In particular, electron-photon interactions and electron transport, which are known to be difficult to simulate using Monte Carlo, must be understood. These processes are handled by Geant4 using multiple scattering theory, described further in Section 5. In this section the interactions of electrons and positrons with matter which underpin the majority of the Monte Carlo simulation will be discussed.

Charged particles interact semi-continuously, rather than discretely, as photons do, resulting in continuous energy loss and multiple scatterings. In this section we will consider the passage of electrons through matter, as other charged particles are less relevant to this work. When ^{192}Ir decays via β^- decay, an electron is ejected from the atom. Additionally, the γ-rays that are produced during all nuclear decay transitions of ^{192}Ir will transfer their energy to secondary electrons. These electrons then traverse and interact with the material, depositing energy into the material in a manner dependent on the stopping power of the material and the energy of the electron.

This energy loss of the incident charged particle is described by the mass stopping power, defined in Equation 2.19, which classifies the Coulomb interaction that incident charged particles undergo with orbital electrons and atomic nuclei. A charged particle may interact collisionally, where it transfers a portion of its energy to the material, or it may interact radiatively, where it emits photons such as bremsstrahlung radiation. If the collisional interaction between the incident electron and the atom results in a small energy transfer, the atom may become ionized or undergo atomic excitation, where an orbital electron is raised to a higher energy state. If the collisional interaction occurs between the incident electron and a single orbital electron, the incident electron may transfer a large portion of its energy to the orbital electron, ejecting it from the atom.

The mass stopping power of a material is defined as [9]

$$\frac{S}{\rho} = \frac{dE}{\rho dx} = \frac{S_{col}}{\rho} + \frac{S_{rad}}{\rho}, \tag{2.19}$$

considering both $\frac{S_{col}}{\rho}$, the collisional interactions that an electron undergoes, and $\frac{S_{rad}}{\rho}$, the radiative processes that may occur due to the acceleration or deceleration of the charged particle by the atoms it encounters. The mass collisional stopping power is an important quantity which defines the dose deposited by charged particles.

2.4 Dose

The measurement of the dose to a point or volume is the foundation of this report. Given that the biological effect in a tissue, both normal and cancerous, is directly related to the dose deposited in the tissue [14], a correct estimation of the dose to the organs is crucial to any treatment plan.

The dose deposited in a medium is proportional to the amount of energy transferred to the medium, quantified by μ_{tr}/ρ in the case of photons and S_{col} in the case of electrons. Using these quantities, the dose for a given radiation field may be calculated.

2.4.1 Radiation Field

Recalling Equation 2.1, the energy imparted, ϵ is defined using the radiant energy R as [9],

$$\epsilon = R_{in} - R_{out} + \Sigma Q, \tag{2.20}$$

where R is the total energy, excluding the rest mass, carried by a particle ($h\nu$ for a γ, and E_K or T for an electron).

The fluence is defined for a multi-directional radiation field comprising N particles as [9]

$$\Phi = \frac{dN}{da} \tag{2.21}$$

and the energy fluence is defined as [9]

$$\Psi = \frac{dR}{da}, \tag{2.22}$$

where one is considering the energy incident on an infinitesimal spherical surface of area a. The use of a sphere in these definitions emphasises that the area da is considered to be perpendicular to the direction of each particle [10].

2.4.2 Indirectly Ionizing Radiation

Indirectly ionizing radiation such as photons deposit dose in a medium by first transferring energy to secondary electrons within the medium. These electrons then go on to directly ionize and excite the atoms of the material, causing damage to cells. The kerma K (Kinetic Energy Released per unit MAss) is defined in order to quantify the energy per unit mass that is transferred from the photons to charged particles within the material. It is the mean sum of the initial kinetic energies of the charged particles liberated by the uncharged particles in a mass dm, and is written [9]

$$K = \frac{d\overline{\epsilon_{tr}}}{dm}. \tag{2.23}$$

ϵ_{tr} only considers the amount of energy that is transferred to the charged particles, but not where the energy is deposited. Recalling Equation 2.13, we can write [8], [9]

$$K = \Psi \frac{\mu_{tr}}{\rho}. \tag{2.24}$$

As with stopping power, kerma can be separated into collision kerma K_C and radiative kerma K_R, such that [8], [9]

$$K = K_C + K_R, \tag{2.25}$$

where K_R is the fraction of the energy that is transferred from the indirectly ionizing radiation to the secondary charged particles and which is subsequently lost due to radiative processes such as bremsstrahlung radiation, and K_C is the portion of energy which is absorbed by the material, rather than radiated away. The collision kerma is then the important quantity to consider in the calculation of dose; if energy is lost to radiative processes it does not form part of the dose calculation. K_C is defined

as [8], [9]

$$K_C = \frac{d\epsilon_{tr}^{net}}{dm}. \tag{2.26}$$

Here, ϵ_{tr}^{net} is the net energy transferred to the medium.

The mass-energy absorption coefficient can be defined [8], [9],

$$\frac{\mu_{en}}{\rho} = (1-g)\frac{\mu_{tr}}{\rho}, \tag{2.27}$$

where g is the fraction of the energy which is transferred to secondary particles and then lost to radiative processes. The mass-energy absorption coefficient is then the portion of the attenuation which is not subsequently radiated away.

It then follows that we can write [9]

$$K_c = \Psi\frac{\mu_{en}}{\rho}. \tag{2.28}$$

The number of radiative interactions that occur is dependent on the atomic number of the material, and so g, $\frac{\mu_{en}}{\rho}$ and K_C are also dependent on the composition of the materials encountered along the path of the secondary electron as it comes to rest. The radiative component of the kerma is also dependent on the photon energy.

Radiation equilibrium exists if for every particle leaving a volume, an identical one enters. Charged particle equilibrium is the application of this concept to charged particles; that is, $(R_{in})_c = (R_{out})_c$. Radiation equilibrium implies charged particle equilibium, but not vice versa. Under charged particle equilibrium, dose is equivalent to the collision kerma [9];

$$D_{med} = \frac{d\bar{\epsilon}}{dm} \overset{CPE}{=} \frac{d\bar{\epsilon}_{tr}^{net}}{dm} = K_c, \tag{2.29}$$

and for a spectrum of energies;

$$D_{med} = K_c = \int_{E=0}^{E_{max}} \Psi_E(E)\left(\frac{\mu_{en}(E)}{\rho}\right)dE. \tag{2.30}$$

The absorbed dose due to indirectly ionizing radiation then occurs in two steps. Initially, energy is transferred as kinetic energy from the photons to the secondary charged particles. This results in kerma. In the second step, these secondary charged particles (electrons) transfer some of their energy to the medium, resulting in absorbed dose, and some of their energy is lost to radiative processes. As electrons traverse a medium and deposit energy along their tracks, this absorption of energy resulting in dose does not occur at the same location as the initial transfer of energy, or kerma.

2.4.3 Directly Ionizing Radiation

In the case of charged particle radiation, such as electrons, we define cema C (Converted Energy per unit MAss) as the analogous quantity to kerma. Remembering that the mass collisional stopping power is the

amount of energy lost by charged particles via collisional interactions, cema is defined as [8], [9]

$$C = \frac{dE_c}{dm}, \tag{2.31}$$

where dE_c is the energy expended by ionizing charged particles other than δ-rays in electronic collisions in a mass dm. Cema explicitly excludes energy losses by these δ-rays in the evaluation of dE_c since their full energy is accounted for in the evaluation of S/ρ; C is essentially the energy transferred to the δ-rays. We can write [9]

$$D_{med} \overset{\delta-eqm}{=} \int_0^{E_{max}} \Phi_E(E) \frac{S_{col}(E)}{\rho} dE = C, \tag{2.32}$$

where the requirement is δ-ray equilibrium.

In the remainder of this report, the dose to a volume of material will be a key concept, as it is the quantity related to the biological response of both normal and cancerous tissue to ionizing radiation, discussed in the following chapter. Using a Monte Carlo simulation, the dose will be calculated from its simplest definition, Equation 2.1, and will be compared to a calculation based on a simplifying equation stipulated in the AAPM TG-43 protocol, which defines the dose as a product of factors specific to the clinical scenario. As it is nearly impossible to measure the dose at a point within a patient's body, it is critical that dosimetry theory is well understood so that dose distributions within a patient may be accurately simulated.

Chapter 3

Brachytherapy

Brachytherapy is a type of localised radiotherapy which is delivered through the use of a radioactive source placed inside or very close to the target volume, facilitated through the use of catheters or applicators [15]. The aim of brachytherapy is the delivery of a planned dose to the tumour or cancerous lesion while providing maximum sparing of the surrounding normal cells [7], in contrast to external beam radiotherapy, where in general a larger volume of normal tissue will recieve a significant dose [15]. Sparing of normal cells is defined as the delivery of a minimal dose to the healthy tissue surrounding the cancerous lesion. Damage to normal cells due to ionizing radiation could induce secondary cancers, or could lead to the organ ceasing to function correctly or entirely. These healthy organs surrounding the cancerous lesions which are located in the radiation field are termed organs at risk.

In order to achieve a high dose gradient which keeps the absorbed dose relatively local, brachytherapy relies on the inverse square law followed by all electromagnetic radiation, which states that the intensity of the radiation is inversely proportional to the square of the distance from the source [16]. When a source emitting ionizing radiation is placed in close proximity to a cancerous lesion, this phenomenon allows for a high dose to be delivered to the tumour and a much lower dose to be delivered to the organs at risk. This means that brachytherapy is able to deliver a much higher dose to the tumour while still keeping the dose to the organs at risk at an acceptable level.

3.1 Radiobiology

The interaction of ionizing radiation with biological cells may result in cell-killing of both normal and tumour cells. The DNA is the target for radiation-induced cell-killing, since if the DNA cannot be accurately repaired, the cell is likely to die. The aim of curative radiotherapy is local control, which is defined as the failure of the tumour to regrow within the patient's lifetime. Local control is achieved via the inactivation of the tumour's clonogenic cells, which are the cells which have the capacity to divide [14]. The biological effects of radiotherapy on both normal and tumour cells depend on dose distribution and rate, the volume of tissue with which the radiation interacts, and the length of the treatment, amongst other factors [17].

As ionizing radiation traverses the human cell, it interacts mainly with the orbital electrons, ionizing and exciting them as was described in Section 2.3. For 1 Gy of absorbed dose there are over 10^5 ionizations in a given cell of 10 μm [14]. As the electrons slow down, they interact more frequently, leading to clusters of ionizations which are particularly damaging to the cell. These ionization clusters are displayed in Figure 3.1. When these clusters occur within DNA, the cell has difficulty repairing the damage. These

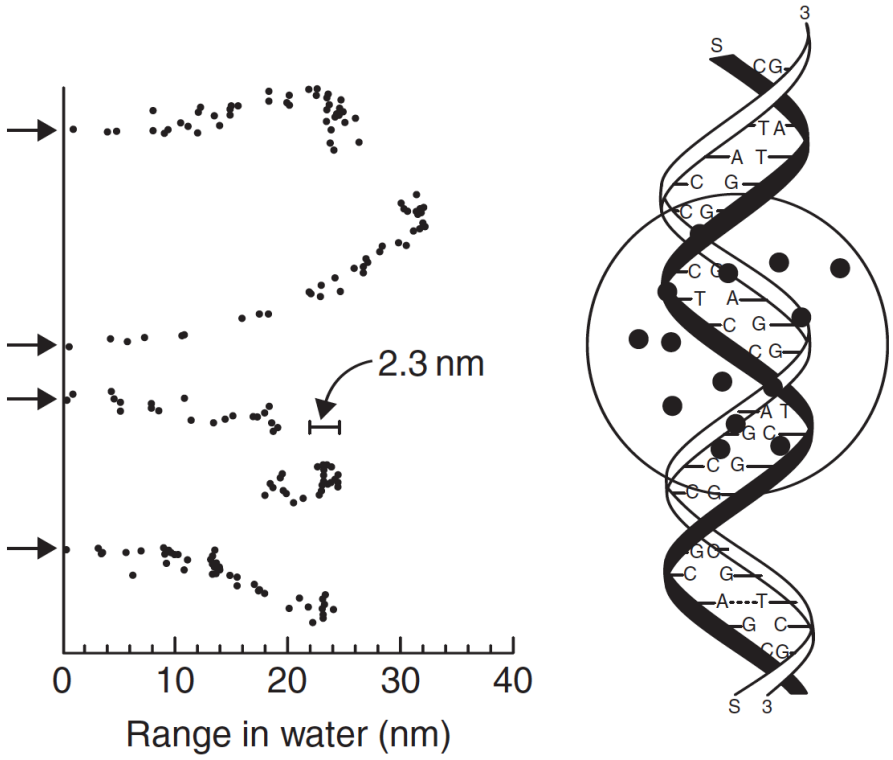


FIGURE 3.1: Computer-simulated tracks of 1 keV electrons showing the size of the clusters in relation to the size of the DNA [14].

ionizations lead to the breaking of chemical bonds within the cell DNA and the creation of free radicals, highly reactive broken molecules which can cause further damage within the cell through the breakage of further chemical bonds, initiating the chain of biological damage. Free radicals interact with oxygen, ultimately yielding the compound $ROOH$ within the target molecule, as is shown in Figure 3.2. This stable chemical change fixes the damage to the DNA [14].

Cell death occurs when the damage repair systems within a cell cannot accurately repair all of the DNA breaks induced by the radiation treatment. When the cell attempts to undergo mitosis, which is cell division used by normal tissue to grow, the abnormality is identified and the cell is not able to multiply. It will then undergo controlled cell death via one of a number of possible processes [14]. While this cell death is intended for the tumour cells only, it is a certainty that normal cells will undergo cell death as a result of the radiation treatment. This can lead to undesirable side effects, which may be relatively minor, such as burns to the skin, or more severe, such as significant damage to the functioning of an organ at risk. The killing of stem cells leads to normal tissue damange, and may also lead to secondary cancers. It is for this reason that radiation damage to surrounding normal tissues should be kept to a minimum during radiotherapy. The possibility of local tumour control and of damage to the normal cells are both radiation dose dependent, so the treatment must be carefully planned in order to achieve the optimal result.

3.2 Brachytherapy for Cervical Cancer

Cervical cancer is the fourth most common cancer among women worldwide, and is the second most common among women in South Africa, where it is also the leading cause of female cancer deaths [18]. The Human Papilloma Virus (HPV), which is sexually transmitted, is the cause of almost all cervical

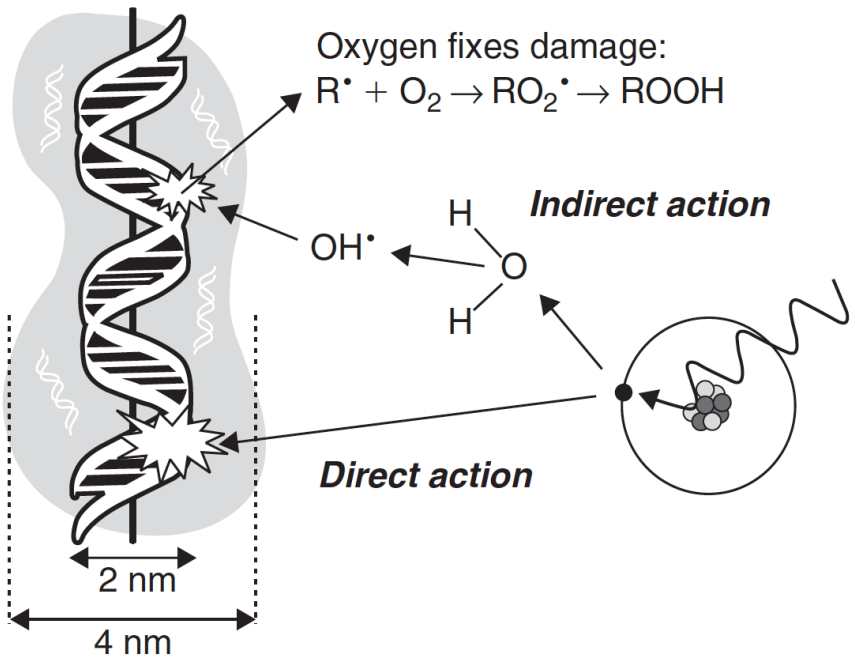


FIGURE 3.2: Creation of free radicals, $R*$, in nearby water molecules, termed indirect action, or within the DNA molecule, termed direct action [14].

cancer [18]. The virus infects the cells of the cervix, leading to abnormal cells which could develop into cancer. Unlike most cancers, cervical cancer can be prevented either through protection against transmission of HPV, or through regular screenings by which the presence of HPV can be detected. While in the early stages, cervical cancer can be treated, but treatment becomes more difficult once the disease has spread.

According to Lim *et al* (2016) [19], the nature of cervical cancer and its cause leads to a greater prevalence of the cancer in developing countries such as South Africa, where socio-economic factors influence diagnosis and treatment of the disease. Although screenings for early detection of precancerous lesions are becoming more readily available in sub-Saharan Africa, they are not widely utilised. This is due not only to the cost of the service, but also to societal constraints such as stigmatisation, lack of spousal support, low level of awareness of the services, and cultural barriers involving possible violation of privacy. A lack of financial and geographical access to health care for much of the sub-Saharan population means that the disease, which is curable, is often left untreated. Given the prevalence of the disease in South Africa, it is vital that the treatment planning for those who are able to be treated be as reliable and accurate as is reasonably achievable.

The standard of treatment for cervical cancer patients combines external beam radiation therapy with brachytherapy, and sometimes with concurrent chemotherapy. The external beam radiotherapy is used to treat surrounding areas which may be subject to metastasis, such as the pelvic lymph nodes. The brachytherapy component is intended for treatment of the cervical tumour, and improves disease control and survival [16].

Brachytherapy may be performed with a high dose rate (HDR) or low dose rate (LDR) source. A radioactive source with a dose rate of greater than 12 Gy/h at the dose specification point [8] is

considered to be an HDR source. HDR sources may only be used in combination with afterloading technology, where the movement of the source is controlled remotely by the hospital staff, due to the high source activity [11]. In recent years there has been an increase in the use of HDR rather than LDR brachytherapy, due to advantages including precise positioning of the source, shorter treatment times, and protection of the staff from radiation exposure due to the use of afterloading technology. There is also no need to hospitalise patients undergoing HDR brachytherapy as they do not pose a danger of exposing the public once the treatment session is over, which is particularly beneficial to limited resource centres. An additional benefit is the possibility of manipulation of the dose deposition distribution using an optimisation of the movement of the source through the applicator [16]. This report will focus on intracavitary brachytherapy, which is the dominant type of treatment performed on cervical cancer patients [3], performed using ^{192}Ir, which is an HDR source.

3.3 Intracavitary Brachytherapy

Brachytherapy for cervical cancer can be performed using an intracavitary technique, where an applicator through the vaginal cavity is used, or interstitial technique, where needle-like tubes are inserted directly into the tissue, the choice of which depends ideally on the disease extent and anatomy. However, the use of interstitial brachytherapy is more specialised, and requires a centre with true expertise [16]. For this reason, lower resource centres such as CMJAH perform only intracavitary brachytherapy. High dose rate intracavitary brachytherapy for the treatment of cervical cancer is performed by the insertion of a radioactive source into the vaginal and uterine cavities, using a specialised applicator. It is the most common brachytherapy technique in patients with cervical cancer [3].

A wide variety of applicator designs exist for use in intracavitary brachytherapy. At CMJAH, the applicator is in the form of a tandem and ring. The tandem is a long straight catheter which extends through the cervix into the uterus, and the ring-shaped catheters accompanying the tandem sit flush against the cervix. The source then moves through the catheters. This is intended to place the source in close proximity with the cervical tumour, as well as any extra-cervical extensions of the tumour. An example of the tandem and ring applicator system used at CMJAH is shown in Figure 3.3.

3.3.1 Afterloading Technology

The afterloading technology used at CMJAH for treatment delivery is the GammaMed Plus system, which has a specific source design, which is further discussed in Section 5.2. A remotely controlled afterloader allows for the source to be transported from its shielded housing into the applicator, under the control of a staff member who is not in the room. The afterloader comprises of a shielded source housing, where the source is kept when it is not in use, and a long steel cable with an iridium source attached at the end of it. This cable can be extended and retracted remotely. While the source is still housed in the shielded container, the chosen applicator is inserted intracavitarily by the hospital staff, who then leave the treatment room, and the ^{192}Ir source, is inserted into the catheter [16].

The source is then moved through the catheters, stopping at predefined dwell positions for predefined dwell times summing to an application duration of minutes [11]. Given that the source steps through the



FIGURE 3.3: Intracavitary brachytherapy applicator employing a tandem and ring system [20].

catheter in this way, the dose to a given point is then the sum of the dose rate due to the source at each dwell position, multiplied by the dwell time at that point. Different configurations of dwell times and dwell points will clearly yield different dose distributions in the surrounding tissue, and an optimisation is performed by the treatment planning system in order to find the best suited dwell pattern.

Chapter 4

Treatment Planning and Reporting Standards

Treatment planning in brachytherapy has developed at a much slower rate than that of external beam radiotherapy, as in many centres brachytherapy plans are not fully specified to the patient and the dosimetry used is based on simple algorithms and calculations which have been in use for many years. The European Society for Radiotherapy and Oncology Booklet no. 8 (2004) [15] cites that the difficulty in delineation of the target volumes and lack of resources, combined with a lack of calculation algorithms which take into account tissue heterogeneities or prescribe to an organ according to its volume rather than to a point, have meant that brachytherapy dosimetry has experienced very little development in the last 30 to 40 years. In particular, limited resource centres such as CMJAH are resigned to using semi-generalised treatment planning systems due to economic and patient volume constraints.

Despite this generally slow development in comparison to external beam radiotherapy, there have been significant developments in the field of brachytherapy in the last decade, including a much higher usage of HDR treatment, and a move towards image-based treatment planning. Higher resource centres with better funding are moving towards Monte Carlo-based planning, as well as including MRI or tomographic images in the planning system, which allow for an improved consideration of the tissues and structures involved in the treatment.

At CMJAH, the planning of a brachytherapy treatment to be performed on a cervical cancer patient is done using the dose calculation formalism outlined in the protocol published in 1995 and revised in 2004 by the American Association of Physicists in Medicine Task Group No. 43 (AAPM TG-43) [4], [21] in order to calculate the dose distribution. The structure of the dose calculation formalism is described in detail in Section 4.1. The recording and reporting of treatments follows the ICRU Report 38 [22] protocol published by the International Commission on Radiation Units and Measurements in 1985. The ICRU-38 protocol dictates that the target and organs at risk are represented by points; the cervix is represented by an anatomical reference point named Point A, and anatomical reference points are defined to represent the target organs. This is detailed in Section 4.2.

4.1 Dose Calculation using AAPM TG-43

The AAPM formed the Task Group No. 43 in order to recommend a dosimetry protocol including a dose calculation formalism, initially designed for small LDR interstitial sources but extended to HDR

intracavitary sources. This protocol was initially published in 1995 [21], and has since undergone a revision which was published in 2004 [4], although the majority of the protocol was retained. The revised protocol is summarised here.

The AAPM TG-43 protocol recommends either one-dimensional or two-dimensional formalism for the calculation of the dose to a point, where the former is applicable to a point source and the latter to a cylindrically symmetric line source. A two-dimensional dose calculation will be applied in this work. It approximates the human body as a cylinder of water, meaning that it is then not entirely specific to the patient as the attenuations due to the differing tissue composition of each patient's body is not considered. The protocol takes into account internal and external source geometry, source strength, radiation attenuation and backscatter in order to calculate the dose delivered to the cancerous lesions and the organs at risk. It relies on some source-specific data, published in the protocol and online, including essential functions and factors for a number of sources used in clinical practice.

4.1.1 Two-Dimensional Dose Rate Formalism

The AAPM TG-43 protocol recommends that it be clinically implemented through the use of a computerised radiotherapy treatment planning system. The system simulates the movement of the line source through the catheter, and sums the dose-rate contributions from each point in order to determine the total dose rate, using the two-dimensional dose rate calculation algorithm as given in AAPM TG-43. A line source is defined by the protocol as a dosimetric approximation which considers the clinical source to be a one-dimensional radioactive line segment of length L, along which the distribution of radioactive decay is assumed to be uniform. This approximation is useful in characterising the fall-off of the dose distribution due to the inverse square law, but does not hold as the measurement distance becomes equal to, or less than, the finite width of the source [4]. This is assumed to be a reasonable approximation for the treatment planning purposes.

The two-dimensional dose rate calculation is given in terms of r, the distance in centimetres from the centre of the active source to the point at which the measurement is done, θ, the polar angle specifying the measurement point, r_0, the reference distance (here, 1 cm), and θ_0, which defines the source transverse plane and is specified to be $\pi/2$ radians. The dose rate is written [4]

$$\dot{D}\left(r,\theta\right) = S_K \cdot \Lambda \cdot \frac{G_L\left(r,\theta\right)}{G_L\left(r_0,\theta_0\right)} \cdot g_L\left(r\right) \cdot F\left(r,\theta\right), \tag{4.1}$$

where the subscript L denotes the line source approximation. This is referred to as the AAPM TG-43 dose calculation formalism. This formalism is applicable to sources with dose distributions which are cylindrically symmetric with respect to the source longitudinal axis, which means that it makes an assumption that the sources considered have a cylindrically symmetric dose distribution. The dose-rate contributions from the source to the point(s) of interest are calculated using the two-dimensional dose-rate calculation algorithm given in Equation 4.1, and summed for each position of the source.

The coordinate system is shown in Figure 4.1, where the source of length L is centred at the origin. The reference point $P(r_0, \theta_0)$ is shown. A parameter of importance to the protocol, the transverse plane,

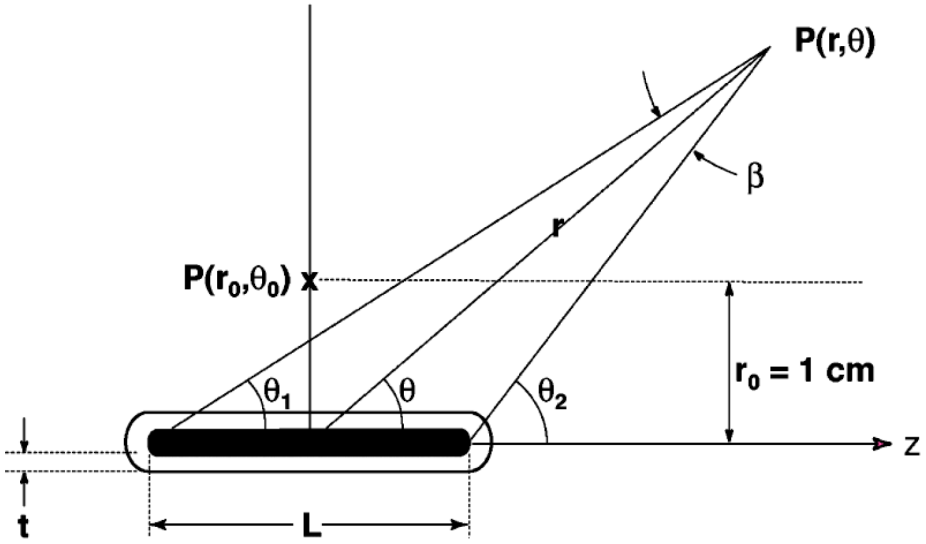


FIGURE 4.1: The two-dimensional coordinate system used by AAPM TG-43 in order to calculate the dose at point $P(r, \theta)$ [4].

bisects radioactive core and lies perpendicular to the longitudinal axis of the source.

The dose rate formalism given in Equation 4.1 depends on several well-defined quantities. The first, S_K, is the air-kerma strength, which has undergone a minor revision in the 2004 update. The air-kerma strength is numerically identical to the Reference Air Kerma Rate (RAKR) which is recommended as the quantity by which sources should be characterised by ICRU-38 and ICRU-60 [23]. The RAKR is defined in ICRU-38 as "the kerma rate to air, in air, at a reference distance of 1 meter, corrected for air attenuation and scattering". Air kerma strength has units of μGy m^2 h^{-1}. S_K is defined as [4]

$$S_K = \dot{K}_\delta (d)\, d^2, \tag{4.2}$$

where $\dot{K}_\delta (d)$ is the air kerma rate *in vaccuo*, meaning corrected for photon absorption and scattering by the air and surrounding materials, where only photons of energy greater than δ are considered in order to exclude contaminant photons, and d is the distance from the centre of the active source to the point of $\dot{K}_\delta (d)$ specification, which is usually but not necessarily the point of measurement. d should be large enough relative to the radioactivity distribution such that S_K is independent of d.

Λ is the dose-rate constant in water and has units of cm^{-2}. It is defined as [4]

$$\Lambda = \frac{\dot{D}\,(r_o, \theta_0)}{S_K}, \tag{4.3}$$

and depends on the radionuclide, source model and internal design. The dose rate constant must be specified as accurately as is possible, as it transforms the AAPM TG-43 dose distribution into accurate dose rates.

The geometry function, $G_L(r,\theta)$, is defined as [4]

$$G_L(r,\theta) = \begin{cases} \beta/Lr\sin\theta & \text{if} \quad \theta \neq 0^\circ \\ (r^2 - L^2/4)^{-1} & \text{if} \quad \theta = 0^\circ, \end{cases} \tag{4.4}$$

where β is the angle formed when two lines connected to each end of the line source meet at the calculation point.

The radial dose function, g_L, accounts for the transverse dose fall-off which is due to photon attenuation. It is defined [4]

$$g_L = \frac{\dot{D}(r,\theta)}{\dot{D}(r_0,\theta_0)} \frac{G_L(r_0,\theta_0)}{G_L(r,\theta)}. \tag{4.5}$$

The two-dimensional anisotropy function, $F(r,\theta)$, accounts for the variation of the dose with the polar angle, and is defined [4]

$$F(r,\theta) = \frac{\dot{D}(r,\theta)}{\dot{D}(r,\theta_0)} \frac{G_L(r,\theta_0)}{G_L(r,\theta)}. \tag{4.6}$$

In a clinical context, the air kerma strength S_k and Λ should be experimentally measured for each source. Published values of G_L, g_L and F are available for a variety of brachytherapy sources and so do not need to be experimentally measured for sources used in a clinical context. In this report, these parameters will be measured using Monte Carlo simulation.

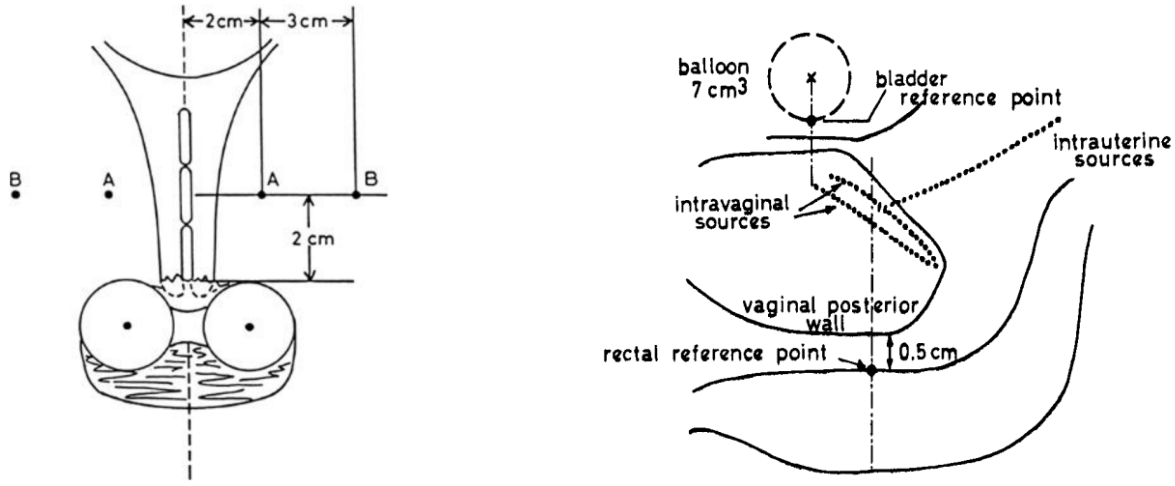
4.1.2 Simplifying Assumptions

Many treatment planning systems employ a number of assumptions, several of which are outlined in the following, which allow the system to be cost and time effective.

In some cases, applicators incorporate shields which are not cylindrically symmetric, but in general treatment planning systems do not take this complex effect into account. In ignoring this additional structure, treatment planning systems also neglect the possibility of intersource back-scatter by this shielding. In this report, a simple cylindrically symmetric applicator is used, with no additional shielding. Tissue heterogeneity, such as the presence of bony structures, lower density cavities such as the lungs or the bladder, and the non-water equivalence of body tissues may influence the dose distribution in the body, but treatment planning systems assume that the body is water equivalent, assuming that tissue heterogeneity may be ignored due to the inverse energy fall-off of the dose distribution around the source [15].

Most treatment planning systems also do not account for the transit dose that occurs between dwell positions and during source entry and exit from the patient. Transit dose, which is dependent on the parameters of the clinical application, can vary from being negligible to a several percent dose discrepancy [15].

Treatment planning systems, which are not completely personalised due to these factors, are not able to provide a completely accurate dose description. The use of the AAPM TG-43 dose calculation formalism, in place of a fully Monte Carlo-based calculation of the dose, means that the dose calculation relies on



(A) Points A and B as defined in the Manchester system [22].

(B) ICRU recommended surrogate points for the rectum and bladder [22].

FIGURE 4.2: Recommended absorbed dose calculation points for critical structures.

approximations and predetermined factors. Customised three-dimensional dose distributions are preferable to generalised planning based on two-dimensional calculations, improving local control and reducing complications [3].

4.2 Recording and Reporting

A patient undergoing brachytherapy treatment should undergo precise treatment planning, and their total dose prescription and dose schedule should be clearly denoted and recorded. Radiation centres follow protocols denoting the treatment prescription, including how to demarcate the target and organs at risk. At CMJAH, ICRU-38 is the reporting protocol which is followed. A brief description of the clinical identification of the target and the organs at risk will be given here, as they are relevant to the optimisation section of this report.

ICRU-38 describes the use of four points labelled Point A and Point B on the left and right, defined in relation to the patient's anatomy and depicted in Figure 4.2a, for the demarcation of the cervical target. The dose to these points then represents the dose to the entire target. Point A is the most common prescription point due to extensive data linking the dose delivered to Point A to tumour control. In fact, ICRU-38 recommends that a target volume should be delineated and prescribed to, rather than target points such as Points A and B, but it describes the use of a point no less.

At CMJAH, Points A and B are used for prescription. Point A is defined as 2 cm superior to the vaginal applicator surface and 2 cm lateral to the uterine canal [11]. Point B is defined as 2 cm superior to the vaginal applicator surface and 5 cm lateral to the uterine canal.

ICRU-38 recommends that the dose to the organs at risk, namely the bladder and the rectum, be calculated using representative points defined from two perpendicular radiographs; anterior-posterior and lateral. The doses to these surrogate points, depicted in Figure 4.2b, represent the dose to the entire

organ.

In the optimisation performed in this report, reference points were used to represent the cervix and a representative organ at risk. Given that the reference points used clinically rely on the anatomy of the patient, reference points for the simulation in this report were identified using estimated distances.

Chapter 5

Monte Carlo simulation using Geant4

Monte Carlo simulations are computational algorithms which rely on random numbers and repeated sampling to simulate processes involving random behaviour [24]. Since radiation transport and emission processes are inherently of a stochastic nature, Monte Carlo simulation is an ideal method through which to model radiation processes. The simulation is based on the probability distribution functions (PDFs) which encompass all possible attributes of the particle at a point in time. A random number generator controls the sampling of the PDFs. Simulations are useful as a verification of theory, as it is possible to calculate quantities such as dose directly from the energy deposited in each volume, referred to as calculation from first principles, rather than relying on estimations and averages. It is also possible to follow each particle that occurs in the simulation, recording information about it such as its origin and the exact processes that it undergoes, which is not possible when using direct measurements. In this report, Monte Carlo simulations are used to verify the AAPM TG-43 input parameters, to calculate the dose independently of the TG-43 formalism, and to finally to perform an optimisation on a simple brachytherapy treatment plan, which is covered in Chapter 6.

The simulation is performed using Geant4 [6] version 10.03, run on a personal computer with a 2.7 GHz Intel Core i5 processor. It is imperative that a Monte Carlo tool which is to be used in a medical physics application should be able to model complex geometries and media, allowing for accurate replication of experimental setups, and accurately simulate physics processes and interactions over the relevant energy range, for which Geant4 is well suited [25].

5.1 Geant4

Geant4 (GEometry ANd Tracking 4) is a general purpose toolkit for particle physics-based simulations, and a repository of information on physics interactions, pooling data and expertise to make up a set of physics models able to handle interactions of particles with matter spanning a large energy range. It is written in C++ [26], which is a general purpose, object-oriented programming language. Object-oriented programming can be briefly described as using classes which define objects, rather than using functions based on actions as is the case with other programming styles. This class system defines the traits and methods associated to each object, allowing objects which share traits (such as types of particles) to be defined in a common way and at one time, rather than each time they are created.

Geant4 is descended from Geant3, a previous physics simulation written in Fortran. In its current state, Geant4 is a detector simulation program used to model the passage of radiation through matter, allowing for physics experiments in the fields of subatomic, nuclear, accelerator, space and medical

physics communities [27].

In order to extract information from the simulation, such as energy deposited in a given volume, scoring volumes can be defined within the simulation. These volumes, defined by a scoring mesh of variable size, bin number, position, and rotation, can measure physics quantities such as dose and energy deposited. These mesh geometries can be entirely independent of the material geometries defined in the simulation [28].

Geant4 accepts input via the command line, or via a macro-based input. Macro files are files which contain user input commands regarding the parameters for a given simulation, and may define geometries, scoring meshes, or the number of decays that the simulation should undergo. In particular, Geant4 macros were used to send consecutive commands to the source in the optimisation section of this report, instructing it where to move to, and for how long.

5.1.1 Particle Transport

Particle transport is handled by Geant4 in a stepwise manner, taking into account physics processes and transportation processes occurring in each step [29]. A given particle is initially simulated by a primary track. A particle track in Geant4 is a snapshot of that particle. Each track is updated by a step, which represents how the particle moves and if it interacts with its surroundings. At the beginning of a step, each active discrete or continuous process must propose a step length based on the interaction the particle undergoes under the process. The shortest of these step lengths is chosen, and the processes are all allowed to continue [30]. Once the process associated to that shortest step length is completed, or another process interrupts it, the step ends, and a new process is simulated. A track can then be thought of as an addition of steps.

Processes are interactions that the particle undergoes with its surroundings, and are grouped into electromagnetic, hadronic, or decay processes. The Geant4 Electromagnetic Physics model handles lepton, photon, and muon interactions including Compton scattering, multiple scattering, annihilation, ionization, and bremsstralung production. The occurrence of these processes is decided according to their cross-section, the particle characteristics, and distance travelled by the particle. A given process is responsible for when and where the interaction will occur, and for generating the final state of the interaction, such as any changes in momentum or secondary particles. Particle transportation, by which the particle interacts with a given material or field, is also defined as a process. Processes may be continuous, such as Cerenkov radiation, or discrete, such as a decay. A given particle can have one or more processes assigned to it at any given time. In Geant4, this is handled by the C++ process class [29]. Thanks to its low energy extensions, Geant4 is highly suitable for experiments in the medical physics domain [25].

5.1.2 Particle Interactions

The photon interactions considered in this simulation are Compton scattering, the photoelectric effect, pair and triplet production, and Rayleigh scattering. The simulation uses a condensed history technique for the simulation of charged particle transport, using multiple scattering theory [29]. Because an electron

undergoes so many Coulomb interactions, we cannot explicitly simulate electron transport interaction by interaction. This is handled by the condensed history technique, taking advantage of mathematical steps in which the effect of a large number of electron interactions are grouped together. These groupings handle the large number of deflections caused by elastic scattering, using multiple scattering theory, and the large number of small energy losses through a continuous slowing down approximation model [31]. Multiple scattering theory handles the cumulative effect of many small angle deflections, contributing to an overall deflection from the original particle direction. The considered interactions for electrons and positrons include bremsstrahlung, Coulomb scattering, and annihilation. Electrons may also undergo ionization, of course.

5.2 Gammamed Source Simulation

The afterloading technology used at CMJAH for treatment delivery is the GammaMed Plus system, which has a specific source design, featuring an ^{192}Ir core encapsulated by a metal shell, as depicted in Figure 5.1. A source is defined in AAPM TG-43 [4] as encapsulated radioactive material for use in brachytherapy. The capsule serves to contain the radioactivity, providing the source rigidity, and absorbing any α and β particles produced during the decay. This leaves a spectrum of γ rays, produced by the decay of the source, as well as characteristic x-rays produced during the decay of source or during the interaction of decay products with the source capsule, to make up the radiation fluence from a brachytherapy source. The GammaMed iridium source was reproduced in Geant4 according to manufacturer specifications, as depicted in Figure 5.2.

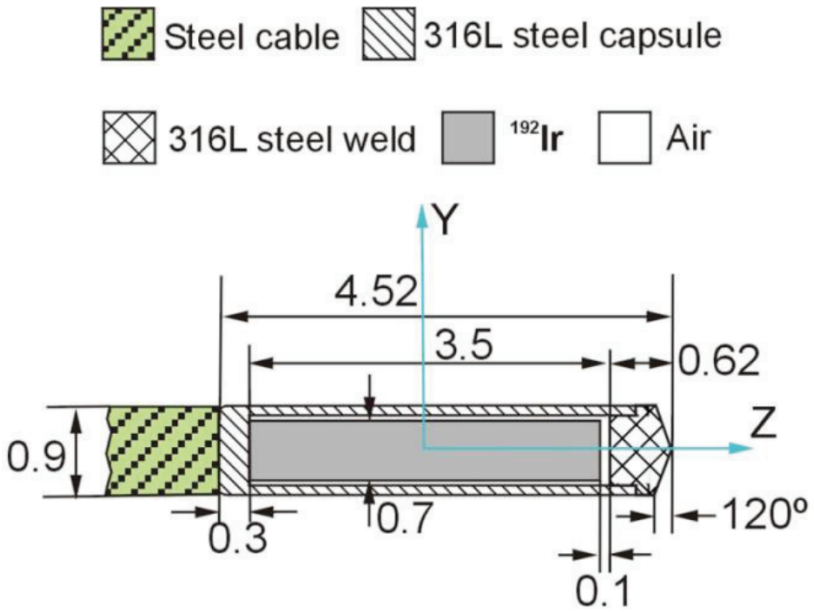


FIGURE 5.1: Materials and dimensions (mm) of the GammaMed source [32].

The GammaMed Plus source features a cylindrical ^{192}Ir core of length 3.5 mm and diameter 0.6 mm sitting within an air pocket of length 3.6 mm and diameter 0.7 mm, encased by a cylindrical stainless steel shell. The stainless steel was simulated as having a density of $\rho = 8.02$ g/cm^3. The shell has an internal diameter of 0.7 mm and an external diameter of 0.9 mm. It has a maximum length of 4.52 mm,

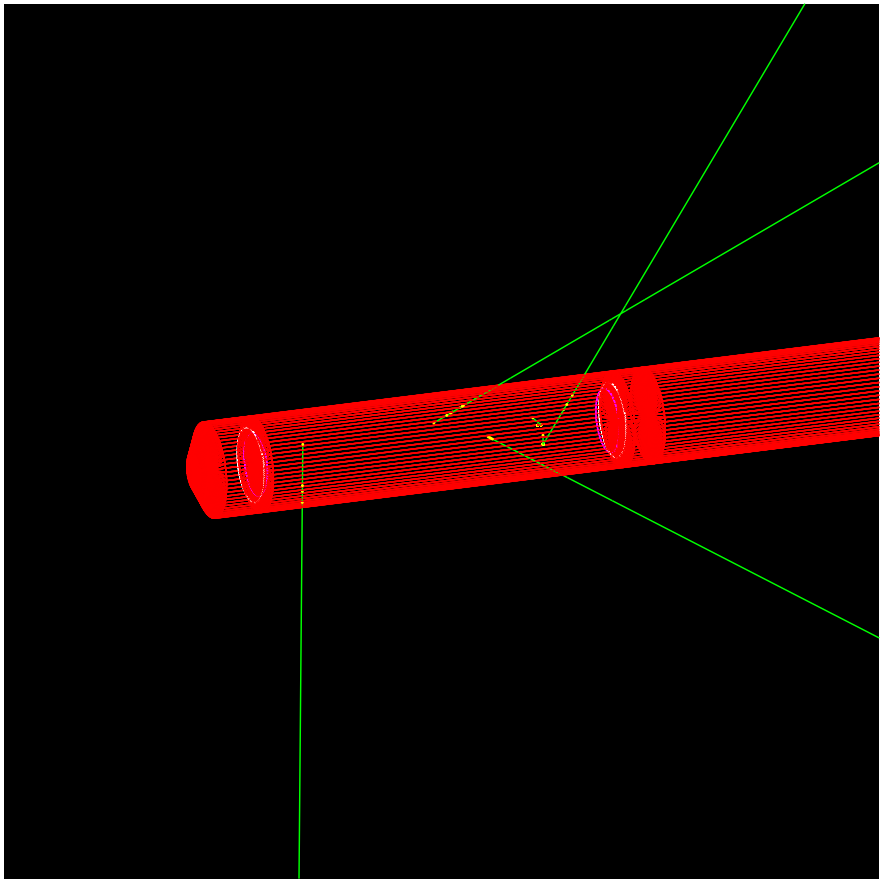


FIGURE 5.2: Simulation of the GammaMed ^{192}Ir source in air where the iridum core and capsule details are visible.

and a truncated cone end. The shell is directly welded to a stainless steel cable of radius 0.9 mm. It is assumed that the radionuclide is uniformly distributed within the core. During simulation, radiation is generated arbitrarily, in a uniform and isotropic distribution, within the ^{192}Ir core, according to the decay scheme of the radioisotope. The radiation emitted by the source is controlled by the user via the number of decay events simulated.

The simulation is shown in Figure 5.2, where the source was simulated in air. In these images, 5 decay events were simulated. In the images, the stainless steel is drawn in red, the outline of the iridium core is visible in magenta, and the outline of the air pocket is visible in white. The γ rays, represented in green, are emitted randomly from the iridium core. The yellow dots are the step points used by Geant4, indicating the next step to be added to the track.

A number of checks were done on the simulated source in order to validate that it was behaving as expected; the source energy spectrum was plotted and compared to reference data, the normalised dose rate was plotted against reference data, and the source was calibrated. These are described in Sections 5.2.1, 5.2.2 and 5.2.3. Once these checks had been satisfactorily completed, the remainder of the simulation was carried out.

5.2.1 Source Energy Spectrum

The primary energy spectrum of the source emissions was recorded for the simulation of 2.8×10^8 histories, and is plotted in Figure 5.3. The primary emission spectrum is measured by running through each track of the simulation when it is no longer active. This occurs when a particle is absorbed by the material (as can occur with photons in processes such as the photoelectric effect), when a particle deposits all of its energy to the material, or when the particle leaves the volume of interest [5]. For a given inactive track, a method is employed to run through each of the particles originating from or attached to that track. If the particle is a γ, the creator process is retrieved, and if the γ originated from radioactive decay the kinetic energy of the γ is saved to the one-dimensional histogram plotted in Figure 5.3.

This primary energy spectrum has been compared to published simulated ^{192}Ir spectra such as the data published by Medich and Munro (2007) [33] (see Table II in the paper), which describes the ^{192}Ir photon spectrum, citing 26 photon energies and intensities which match well with the energies visible in Figure 5.3.

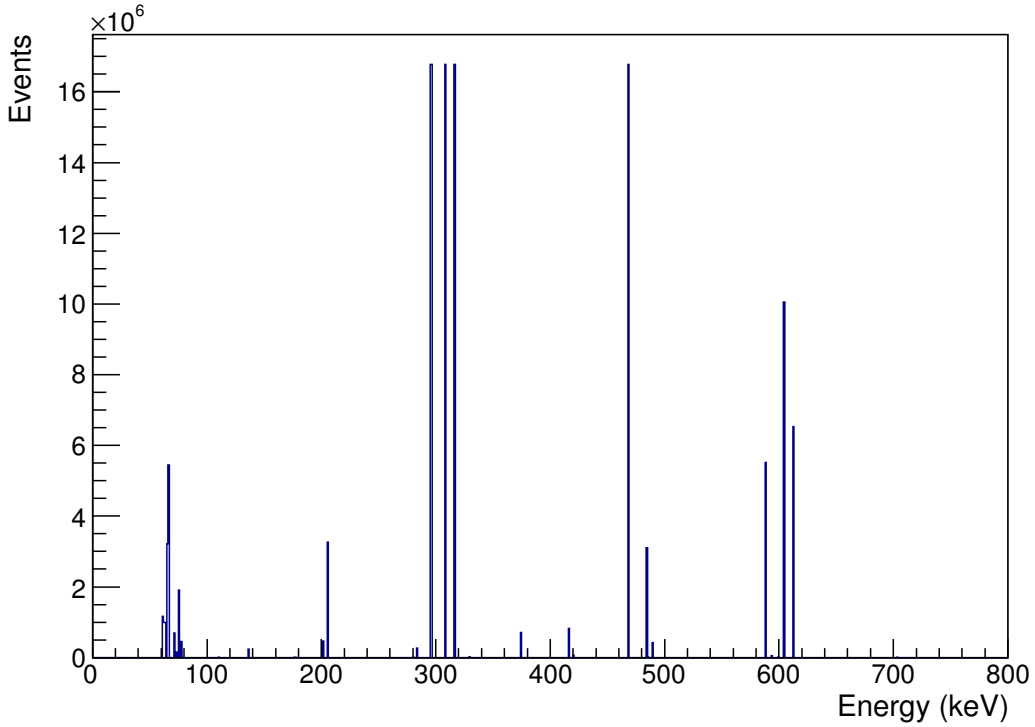


FIGURE 5.3: Energy spectrum of primary particles from the GammaMed source simulated in this report.

5.2.2 Comparison to Reference Data

In order to verify the construction of the GammaMed source and the dose estimation by the Geant4 Monte Carlo simulation, a comparison to reference data was done on the radial dose distribution. The data used was published in *Monte Carlo dosimetry of the most commonly used ^{192}Ir high dose rate brachytherapy sources* (Lopez *et al*, 2011) [34], who used PENELOPE 2008 [35] in order to simulate the AAPM TG-43 parameters for the GammaMed source with a statistical uncertainty of less than 2 % [34].

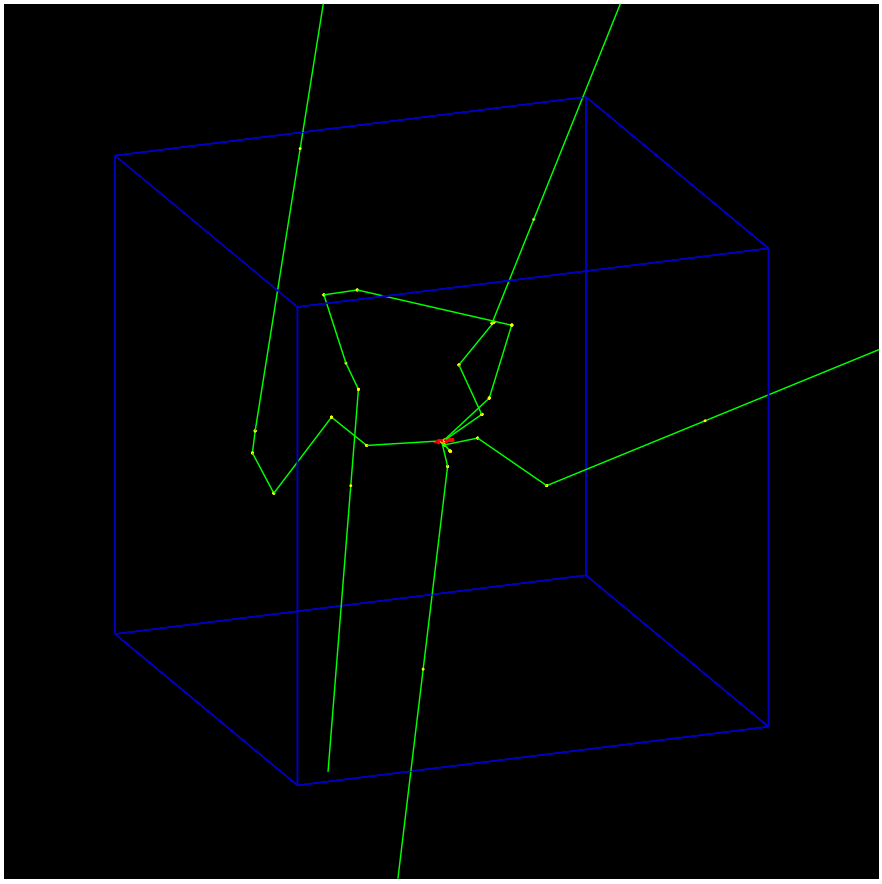


FIGURE 5.4: A depiction of the source undergoing decay events within the water phantom, denoted as a blue cube, used for the dose rate comparison to reference data.

PENELOPE is another general purpose Monte Carlo code used for simulating electron and photon transport. The published results were extensively verified by comparison to other published datasets, in comparison to which the data obtained by Lopez *et al* has a better spatial resolution and a lower statistical uncertainty [34].

In the simulation performed by Lopez *et al*, the GammaMed source was immersed in a cubic water phantom of dimensions $15 \times 15 \times 15$ cm^3, where the water was given a density of $\rho = 0.998$ g/cm^3. The phantom was placed in a vacuum. The source was placed at the centre of the coordinate system. The number of simulated histories was 1.575×10^{10} [34].

In the simulation performed in this report, the source was placed at the centre of a water phantom also with dimensions $15 \times 15 \times 15$ cm^3, where the water is given a density $\rho = 1$ g/cm^3, which too was placed within a vacuum with the middle of the cylindrical iridium source aligned with the origin of the coordinate system. The length of the source was aligned with the z direction, with the positive direction pointing away from the cable. The positioning of the source within the cubic water phantom is shown in Figure 5.4.

The spatial discretisation chosen was cubic cells of 0.25 mm in length, width, and depth, creating a scoring mesh. In order to calculate the radial dose distribution, which is the dose in the $x - y$ direction where the dose at each radius $r = \sqrt{x^2 + y^2}$ is considered, a plane was defined between $z = -0.125$ mm

and $z = 0.125$ mm, extending to the edge of the phantom in the x and y directions. A simulation of 2.8×10^8 histories was run and the energy deposited in each of the scoring mesh cells was recorded and saved in a two dimensional histogram.

After the simulation was completed, the histogram was analysed and the radius associated to each cell in the scoring mesh was calculated. The energy depositions in the cells at corresponding radii were summed and normalised to the number of cells that contributed to the given radius. The energy deposition was normalised to be 1 at 1 cm from the origin of the coordinate system (the centre of the source), as this corresponds to the reference point $r(1\ \mathrm{cm}, 90°)$ indicated in AAPM TG-43.

The normalised distribution is plotted against the data published by Lopez *et al* in Figure 5.5. The normalised radial dose rate was compared to reference data before the source was calibrated, hence the need for both data sets to be normalised to unity at the reference depth. This was done in order to ascertain that the fall-off of the dose distribution was as expected. The data are plotted with statistical uncertainty. The distributions show clear agreement within the statistical uncertainty of the Geant4 simulation.

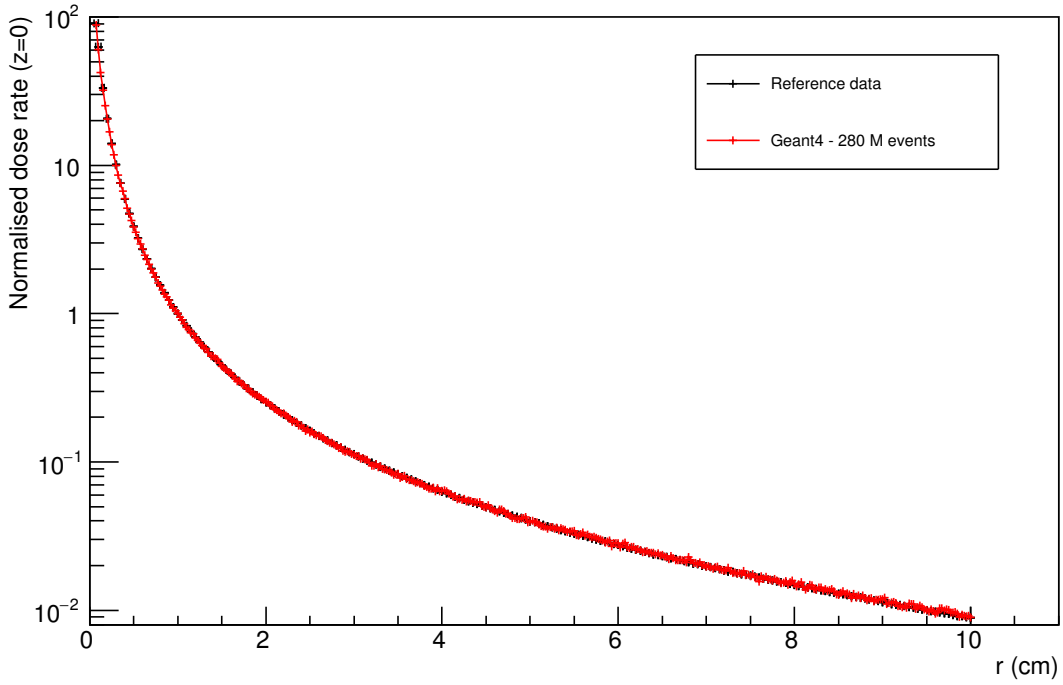


FIGURE 5.5: Normalised radial dose comparison between simulation using Geant4 and published reference data.

5.2.3 Source Calibration

In order to perform a simulation using the Geant4 code, the source is positioned and the number of desired decays of the primary isotope is parsed to the simulation. The simulation does not stipulate the activity of the source, and so the source strength must be related to the number of simulated decays. In order to measure the dose rate, we must have an idea of the time over which the dose is measured. However, time is not a parameter in Geant4. In order to calculate the dose rate, it is necessary to calibrate the source in

order to calculate the number of decays which correspond to a unit of time. The dose rate is necessary for the calculation of the anisotropy function and the radial dose function.

5.2.3.1 Calibration Theory

This calibration is done by nominating the desired source strength, measuring the reference air kerma rate for an arbitrary number of decays, and determining the number of events to be simulated to represent one second of dwell time for the HDR ^{192}Ir brachytherapy source in question. The nominal source strength, rather than the source activity, is used as a starting point for the calibration as it is not valid to convert the activity of a standard brachytherapy source to decays per second in order to estimate the number of γ particles reaching a given point in the material. This is due to the fact that these decays are simulated within the source encapsulation, and so it is not assured that these γ-rays will all reach the point at which the measurement is done.

In order to calibrate the source, we employ the reference air kerma rate (RAKR), as introduced in Section 4.1. It is defined as

$$\dot{K_R} = \dot{K}(d) \cdot \left(\frac{d}{d_{ref}}\right)^2 \qquad [\text{Gy s}^{-1}], \tag{5.1}$$

where $\dot{K_R}$ is the RAKR, $\dot{K}(d)$ is the air kerma rate at a distance d, and d_{ref} is the reference distance of 1 m.

The RAKR is connected to the source strength, S_K, as

$$S_K = \dot{K_R}(d) \cdot d_{ref}^2 \qquad [\text{Gy m}^2\ \text{s}^{-1}], \tag{5.2}$$

for the reference distance of $d = 100\ cm$.

5.2.3.2 Calibration Set-Up

A standard 10 Ci HDR ^{192}Ir brachytherapy source can be expected to have a source strength of approximately 40 mGy m^{2}h^{-1} [36]. In order to measure the RAKR, the simulated source was placed at the centre of a vacuum, and a $10 \times 10 \times 10$ cm^3 cube filled with air at standard temperature and pressure, labelled the critical volume, was centred at a 1 m distance along the y axis. This is visible in Figure 5.6, where two tracks can be seen leaving the source encapsulation. The critical volume is depicted as a white cubic shape, situated 1 m from the centre of the source. The spherical blue phantom is maintained as a vacuum, as is the surrounding world.

5.2.3.3 Calculation of Kerma for Calibration

For the calibration procedure, the source was simulated to undergo a nominal number of decays. Unlike some other Monte Carlo toolkits, Geant4 does not have an inbuilt kerma scorer, and requires the user to program a measurement of the kerma from first principles. In order to measure the reference air kerma rate, each track in the simulation was considered. Each track is associated to its parent track, as shown in Figure 5.7, where the orange track labelled 1 is the primary, or parent, track, and the blue tracks labelled 2, 3, and 4 are the secondary tracks. The green tracks labelled 5 and 6 are not associated to the primary

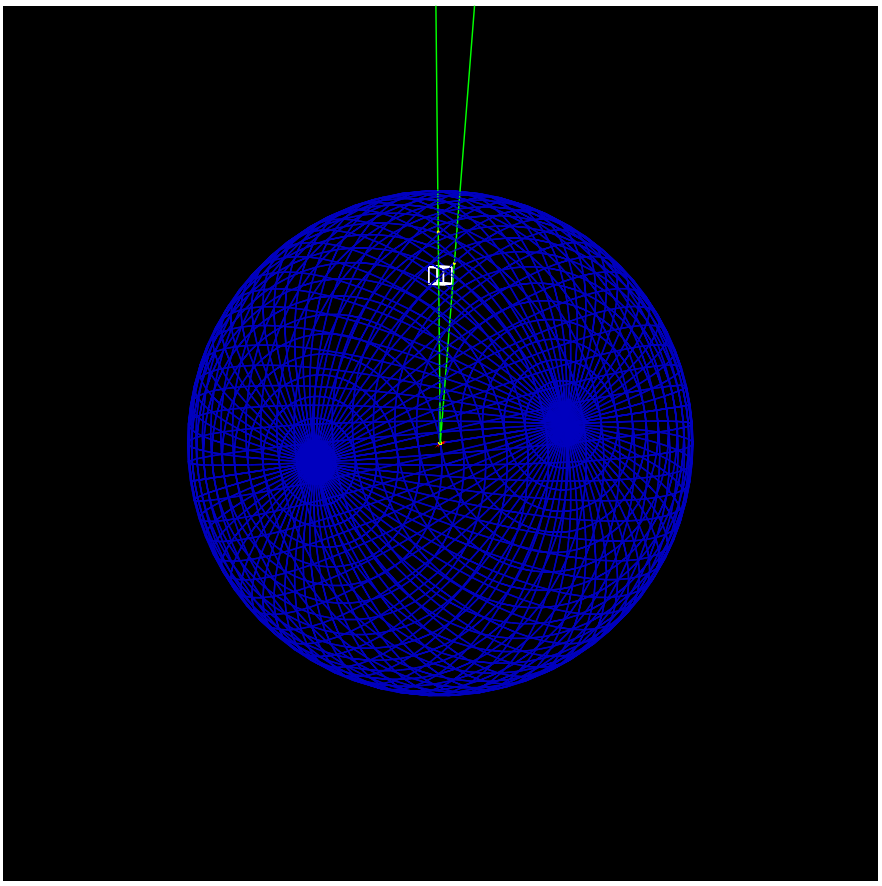


FIGURE 5.6: The geometry used for the calibration process is shown, with 5 decay events simulated.

track. For each track we are able to access the vertex at which that track branched off from the parent track.

In order to measure kerma, of interest are primary tracks which are photons (as shown by the orange track in the figure), and secondary electrons (depicted by the blue tracks in the figure), which are produced when the photon interacts with the material. In order for a track to be considered a secondary electron of interest to the kerma measurement, it is then required to have a non-zero charge, and have a parent track which was produced during radioactive decay. In order to measure the kerma in the critical volume, the secondary electrons whose production vertex was inside the critical volume were considered. The kerma, as defined in Equation 2.23, is then the sum of the kinetic energies released to each secondary electron at their interaction vertex, divided by the mass of the critical volume.

The measurement of the kerma was implemented through the Geant4 Stepping Action Class G4VUserSteppingAction, an optional user action class which is used to define additional actions during the simulation, and which is called at the end of each step along a particle's track. The Stepping Action class has access, at the end of each step, to the particle's tracking and transport history, as well as its characteristics and the complete information about the physical volume in which the step is situated [30]. At each step, then, the particle's charge, parent, position, vertex kinetic energy and the parent's charge and creator process are called.

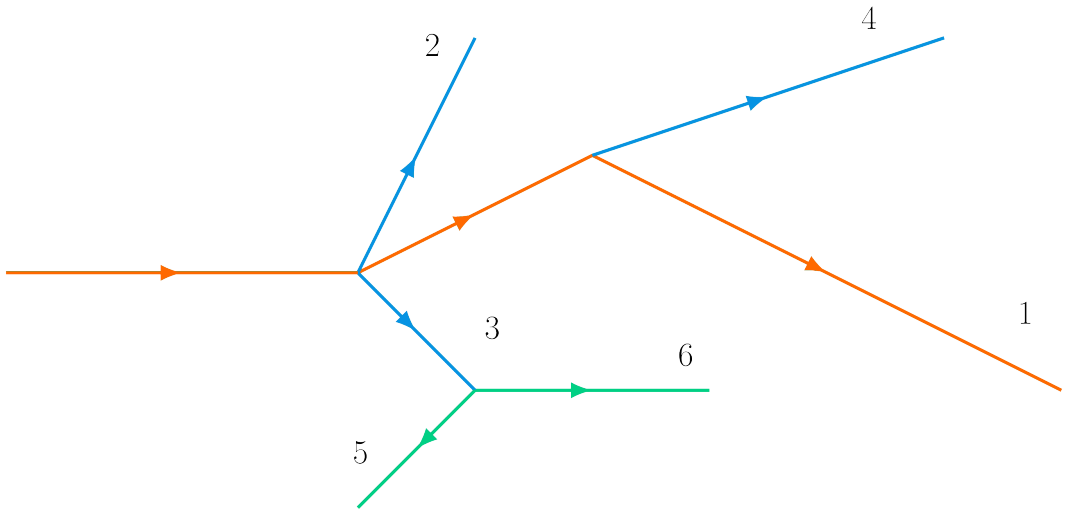


FIGURE 5.7: An example of the assignment of tracks moving through a volume.

5.2.3.4 Calibration Results

2×10^9 events were simulated, yielding an air kerma of 2.44019×10^{-5} mGy. The conversion to time is done using the conversion given in Equation 5.3 at 1 m,

$$\frac{n}{K[\text{mGy}]}\, S[\text{mGy m}^2\text{h}^{-1}] = n\ \text{h}^{-1}\ 1\ \text{m}^2, \tag{5.3}$$

where n represents the number of decays simulated, and S is the source strength. In order to mimic a standard HDR ^{192}Ir brachytherapy source decaying for one hour, it is then necessary to simulate 3.33581×10^{15} decays. In order to mimic a second of decay, it is necessary to simulate 9.26613×10^{11} decays.

As a standard HDR brachytherapy source is usually on the order of 10 Ci = 10×37 GBq = 3.7×10^{11}decays s^{-1}, we would expect on the order of 10^{11} decays to be equivalent to one second. It is in fact expected that the number of decays should be higher than 3.7×10^{11}, given that not all of the γ-rays will escape the source encapsulation; so in order to achieve a source strength of 40 mGy m^{2}h^{-1} we need to simulate extra decays. It is then suggested that the result is reasonable.

The reference air kerma rate is then

$$RAKR = \frac{K(d)}{n} \frac{9.26613\ \times\ 10^{11}\ \text{decays}}{\text{s}} = 0.01131\ \pm 0.00090\ \text{mGy s}^{-1}, \tag{5.4}$$

where the uncertainty was calculated using the standard error,

$$\sigma_{\bar{x}} = \frac{\sigma_x}{\sqrt{N}}. \tag{5.5}$$

The RAKR of a new HDR ^{192}Ir brachytherapy source of approximately 10 Ci is around $0.011337\ \text{mGy m}^2\ \text{s}^{-1}$ [37], which agrees within uncertainty with the simulation.

Recalling Equation 5.2 [38], we then have, from Equation 5.4, that

$$S_K = 40716.0 \ \pm \ 3240.0 \, \text{cGy cm}^2\text{h}^{-1}. \tag{5.6}$$

The calibration allows for the conversion of a dose to a point into a dose rate. The dose rate at the reference point, r = 1 cm and $\theta = 90°$, is measured as 41736.8 cGy/h, yielding a dose rate constant

$$\Lambda = 1.03 \ \pm \ 0.01 \, \text{cm}^{-2}, \tag{5.7}$$

where the uncertainty is a combination of the uncertainties of S_K and $\dot{D}(r_0, \theta_0)$.

5.3 AAPM TG-43 Parameters

For the calculation of the remaining TG-43 parameters, the geometry function, the anisotropy function, and the radial dose function, the source was placed in a semi-infinite spherical water phantom of radius 1 m, which was in turn placed within a vacuum. 2×10^9 events were simulated. The parameters are plotted against reference values in the following, including uncertainties which are described in Section 5.4.2.

5.3.1 Geometry Function $G_L(r, \theta)$

In order to calculate the geometry function G_L as was defined in Section 4.1, we recall the definition

$$G_L\left(r, \theta\right) = \begin{cases} \beta / Lr \sin\theta & \text{if} \quad \theta \neq 0° \\ r^2 - L^2/4^{-1} & \text{if} \quad \theta = 0°, \end{cases} \tag{5.8}$$

where β is the angle formed when two lines connected to each end of the line source meet at the calculation point, as described in Figure 5.8. θ is the angle from the z axis made by a line joining the midpoint of the source (z=0) to the calculation point, θ_2 connects the end of the line source on the positive z-axis to the calculation point, and θ_1 connects the end of the line source on the negative z-axis to the calculation point.

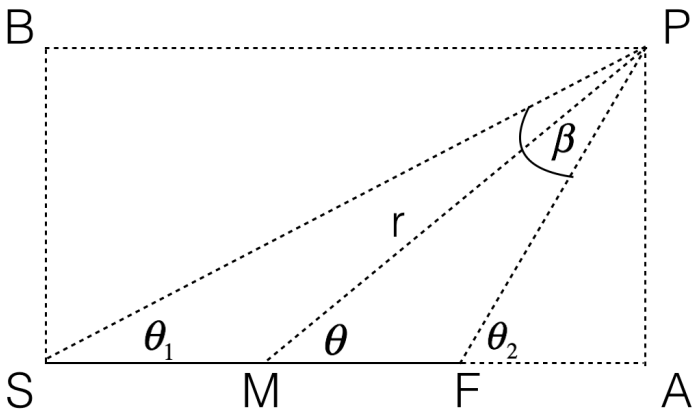


FIGURE 5.8: The geometry relevant to the determination of β, where the source length is $|SF|$, the measurement point is P, and the line $|MP$ joining the source centre to the measurement point has length r.

From Figure 5.8, it is clear that angle $S\hat{P}A = 180° - 90° - \theta_1 = 90° - \theta_1$. Similarly, angle $F\hat{P}A = 90° - \theta_2$. Then $\beta = 90° - \theta_1 - (90° - \theta_2) = \theta_2 - \theta_1$. It is also clear that we can express θ_2 in terms of θ and r, where the distance $|MF|$ is half the length of the source, $L/2$ [39];

$$\theta_2 = \tan^{-1}\left(\frac{r\sin\theta}{r\cos\theta - L/2}\right). \tag{5.9}$$

Using the law of sines [39], we write

$$\frac{\sin(\beta)}{L} = \frac{\sin(\pi - \theta_2)}{|SP|}, \tag{5.10}$$

and since $\sin(\pi - \theta_2) = \sin(\theta_2)$ and by Pythagoras we have [39].

$$\sin(\beta) = \frac{L\sin(\theta_2)}{\sqrt{(r\sin\theta)^2 + (r\cos\theta + L/2)^2}} = \frac{L\sin(\tan^{-1}\left(\frac{r\sin\theta}{r\cos\theta - L/2}\right))}{\sqrt{(r\sin\theta)^2 + (r\cos\theta + L/2)^2}}. \tag{5.11}$$

Then [39]

$$\beta = \sin^{-1}\left(\frac{L\sin(\tan^{-1}\left(\frac{r\sin\theta}{r\cos\theta - L/2}\right))}{\sqrt{(r\sin\theta)^2 + (r\cos\theta + L/2)^2}}\right). \tag{5.12}$$

Once we have β, we can apply Equation 4.4. The geometry function $GL(r,\theta)$ is plotted in Figures 5.9 to 5.10 for values of θ between $0°$ and $90°$.

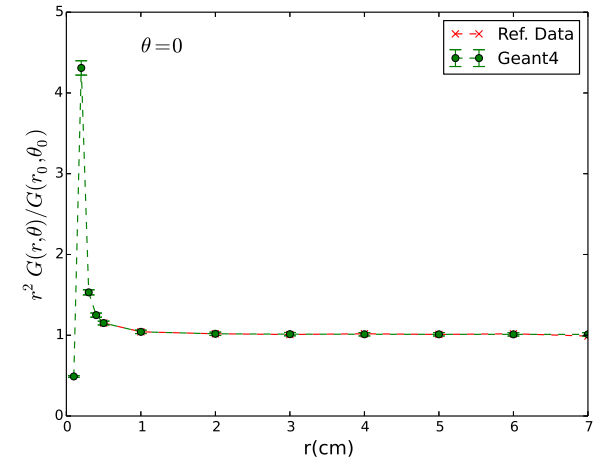
In order to compare the Geant4 calculated values to reference data, the values of G_L were plotted against those given by Reynoso *et al* [40], who calculated the geometry factors for a ^{169}Yb source with a length $L = 3.5$ mm. Given that the geometry function depends on r and θ but not on the source itself, the reference values are comparable to those calculated here.

The reference values are plotted in red, and the Geant4 calculated values are in green. The uncertainty plotted is the combination of uncertainties described in Section 5.4.2, including the standard deviation, which is the statistical uncertainty associated to a point, and the uncertainties on the cross section and emission spectrum. There is good agreement within uncertainty in all plots.

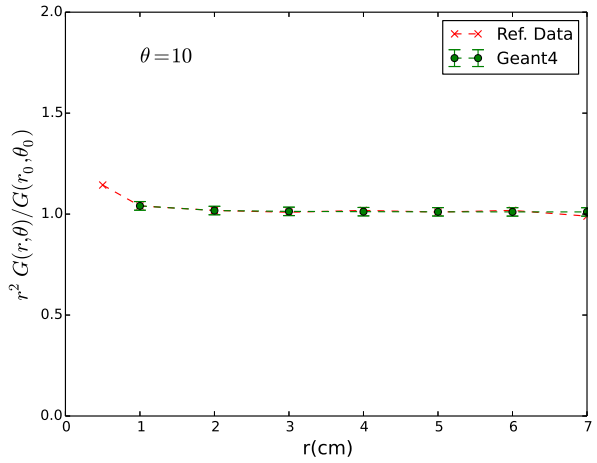
5.3.2 Anisotropy Function $F_L(r,\theta)$

Recalling Equation 4.6, the anisotropy function depends on the dose rate and the geometry function. The updated AAPM TG-43 protocol [4] recommends that $F(r,\theta)$ be plotted from $\theta = 0°$ to $\theta = 90°$ for all sources symmetric about the transverse plane, as is the case for the source in question.

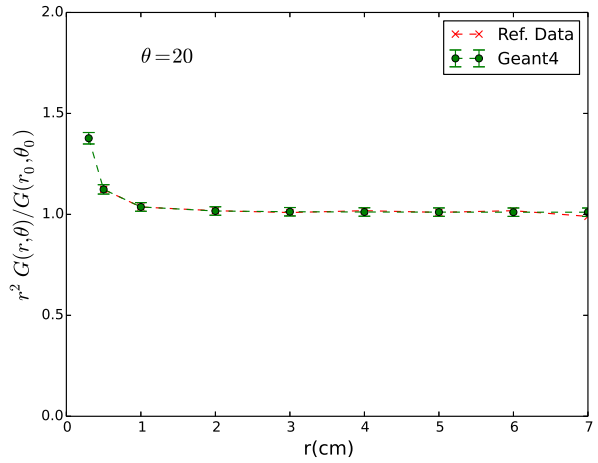
In Figures 5.11 to 5.12, the anisotropy function is plotted between 0 cm and 6 cm radial distance, for values of θ between $0°$ and $90°$. For comparison, the data is plotted in red against reference data plotted in black, published by Ballester *et al* (2011) [41]. The simulated data is plotted including uncertainties as denoted in Section 5.4.2, and the reference data is published without uncertainty. In general there is reasonable agreement within uncertainty between the published and simulated results; the simulation of a greater number of events may lead to the decrease in statistical fluctuations, which could improve agreement.



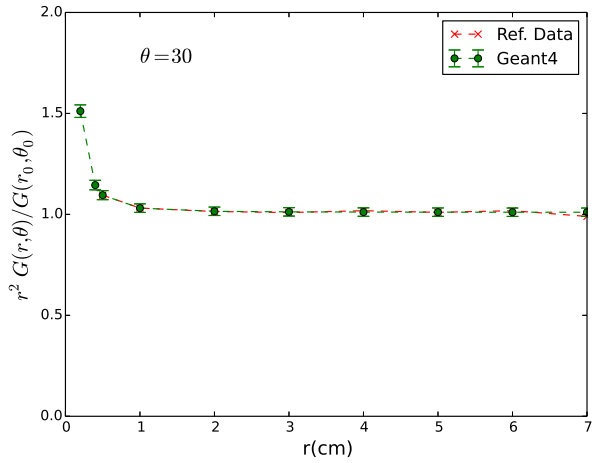
(A)



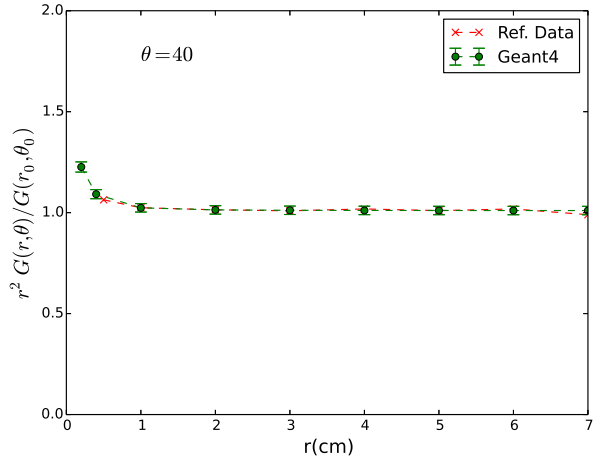
(B)



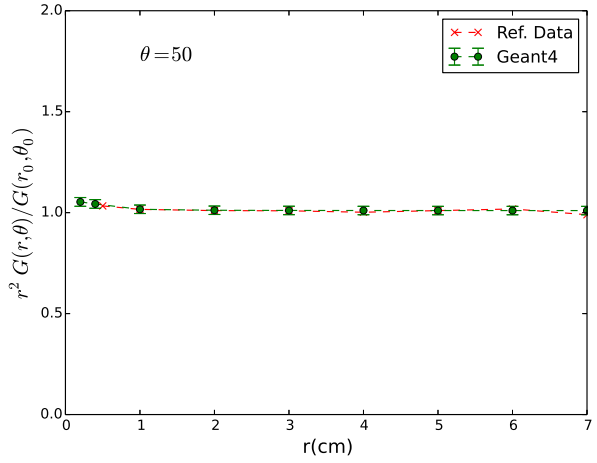
(C)



(D)

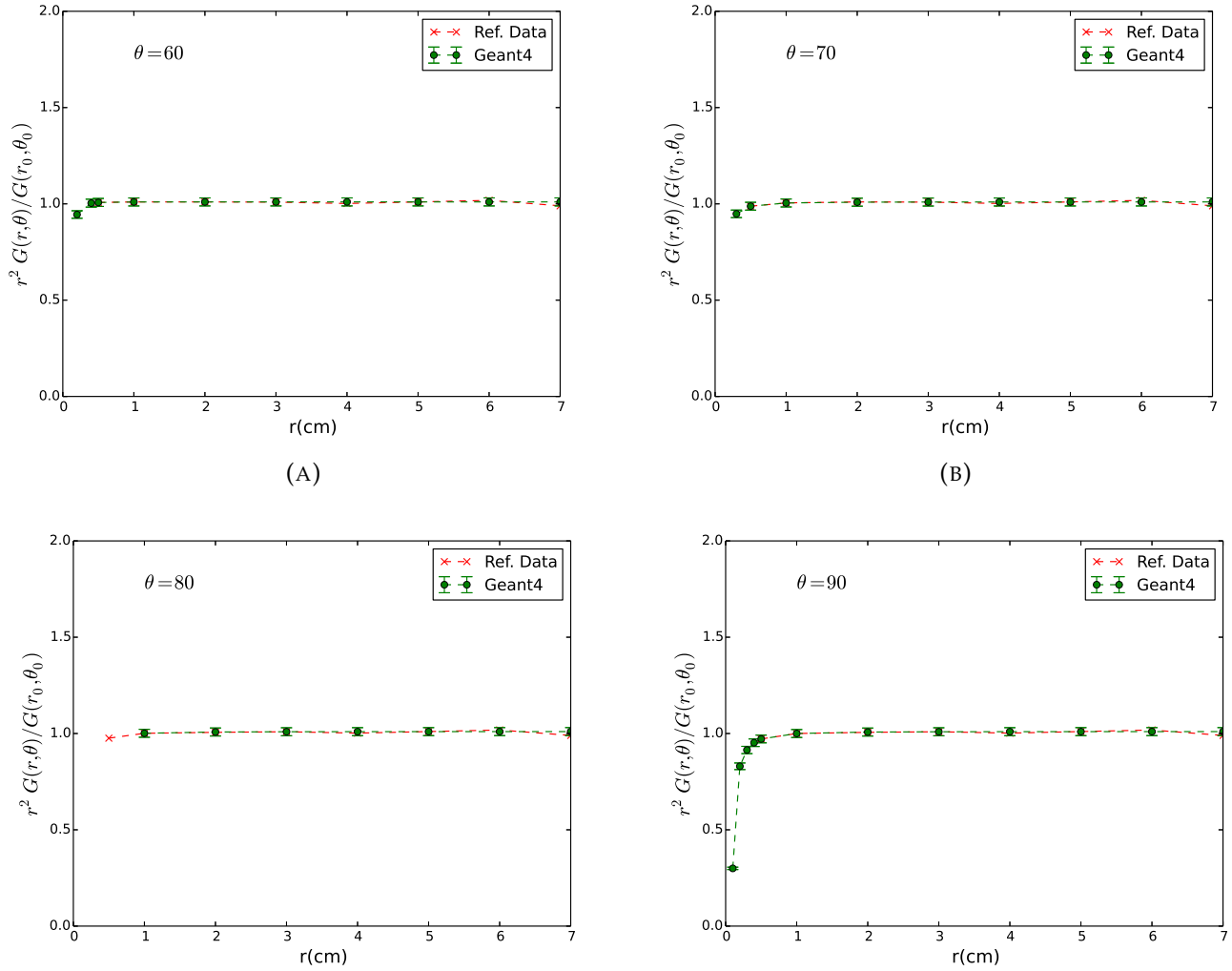


(E)



(F)

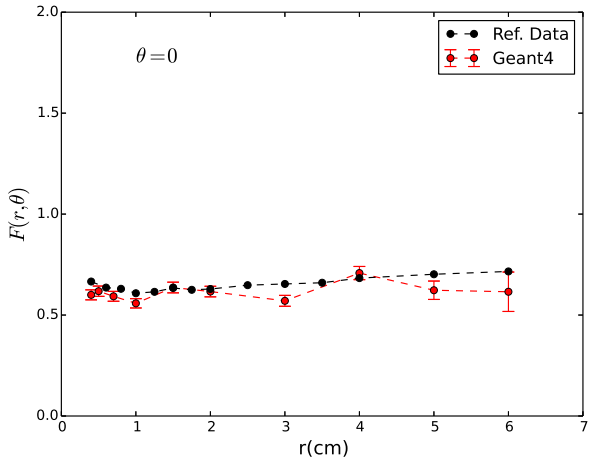
FIGURE 5.9: Values of $r^2 G_L(r,\theta)/G_L(r_0,\theta_0)$ for $\theta = 0°, 10°, 20°, 30°, 40°$, and $50°$.



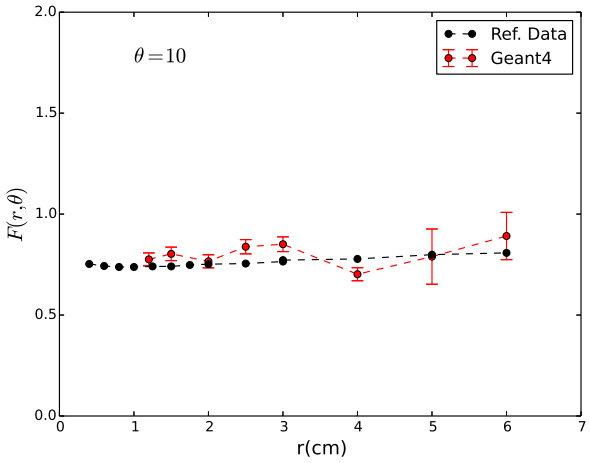
(A) (B)

(C) (D)

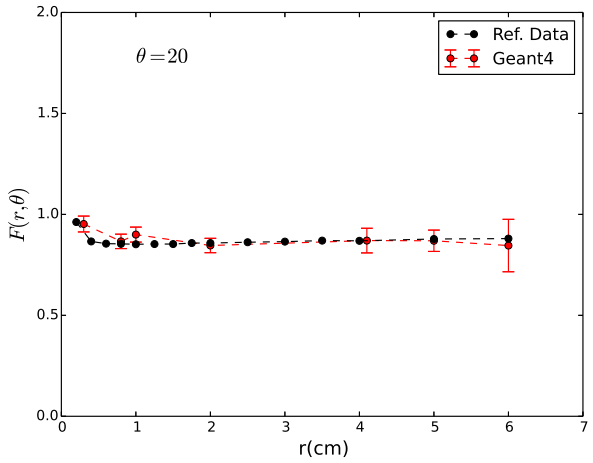
FIGURE 5.10: Values of $r^2 G_L(r,\theta)/G_L(r_0,\theta_0)$ for $\theta = 60°, 70°, 80°$, and $90°$.



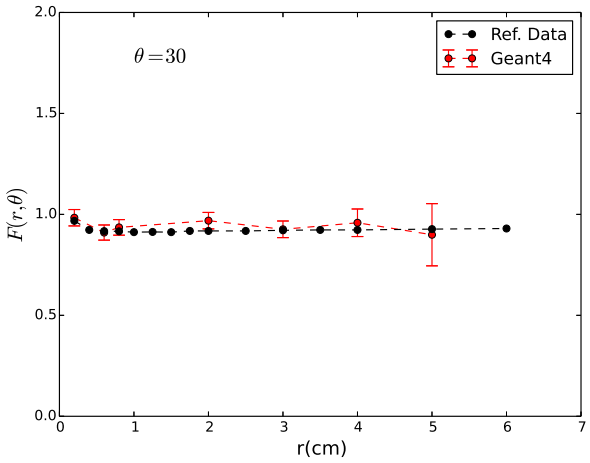
(A)



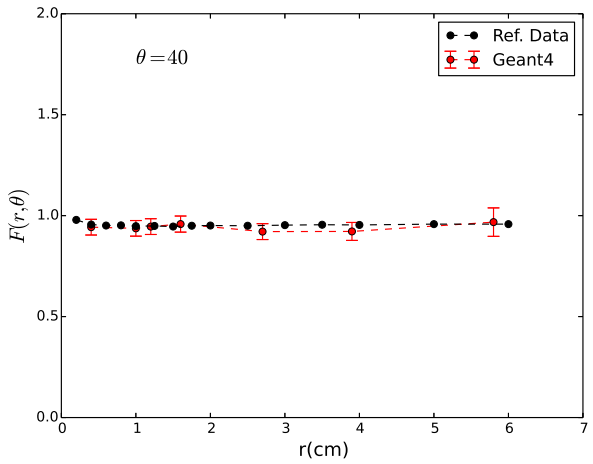
(B)



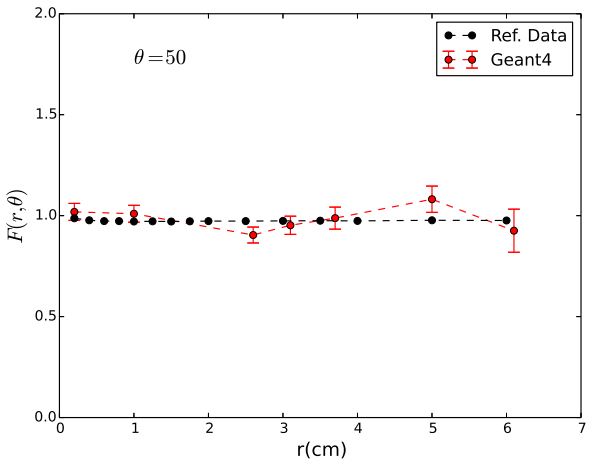
(C)



(D)



(E)



(F)

FIGURE 5.11: Values of $F_L(r,\theta)$ for $\theta = 0°, 10°, 20°, 30°, 40°$, and $50°$.

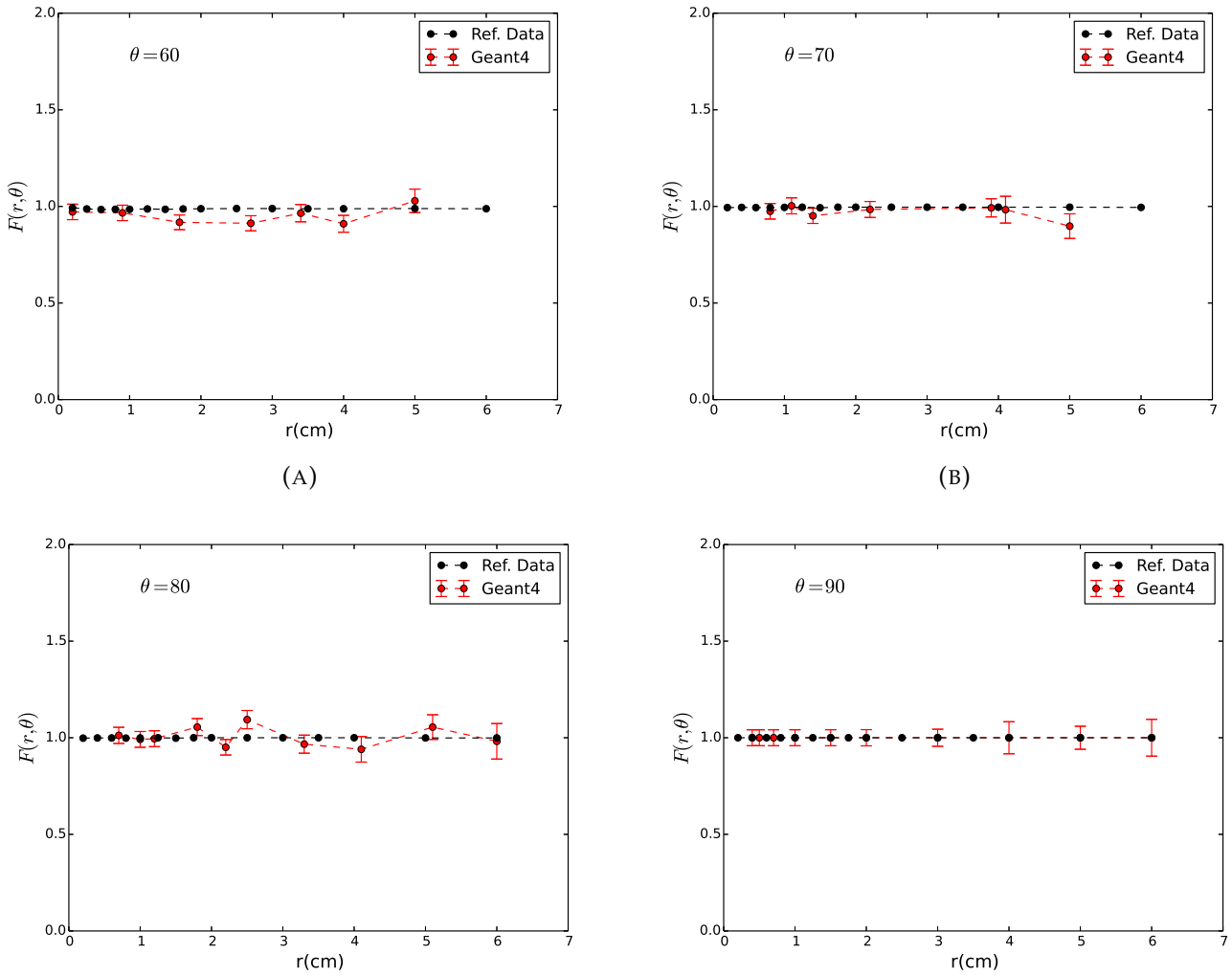


FIGURE 5.12: Values of $r^2 G_L(r,\theta)/G_L(r_0,\theta_0)$ for $\theta = 60°, 70°, 80°$, and $90°$.

5.3.3 Radial Dose Function $g_L(r)$

The radial dose function, $g_L(r)$ is plotted below against reference data from Lopez *et al* (2011) [34] and ESTRO booklet 8 (2004) [15]. There is reasonable agreement within uncertainty between simulation and reference data. The uncertainty plotted on the simulated data is described in Section 5.4.2. As the dose rate falls off quickly with radius, the statistical uncertainty increases sharply, as is visible in the final two uncertainty bars in the simulated data.

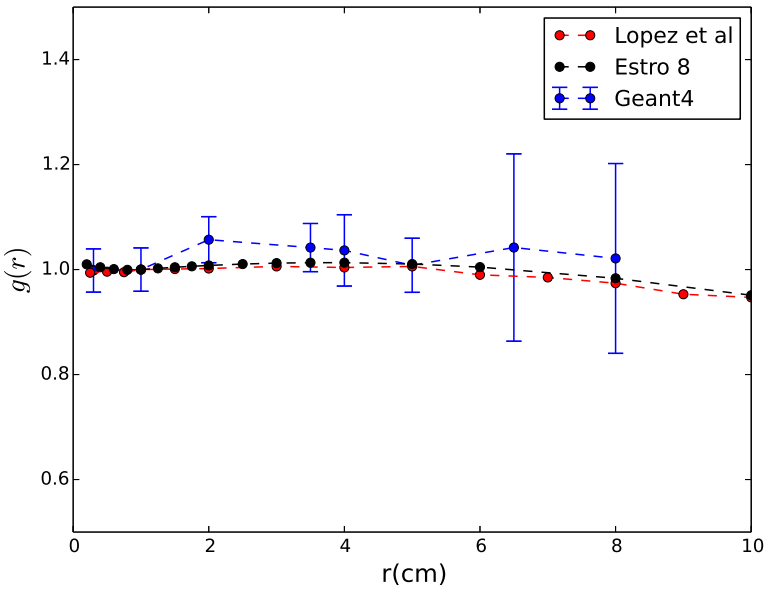


FIGURE 5.13: The radial dose function $g_L(r)$ plotted against reference data.

5.4 Uncertainty

In the following, the uncertainty on the calculated AAPM TG-43 parameters is discussed. A description of counting statistics is given first, as this is a relevant measure of uncertainty on repeated measurements, followed by a discussion of other factors relevant to the uncertainty calculation.

5.4.1 Counting Statistics

In order to assess the uncertainty on a series of repeated random measurements, we can apply statistics to estimate the size of the error on the dataset. In order to estimate the uncertainty on a measurement, we employ the use of counting statistics, which considers a measured count to be a sample from a Gaussian distribution with a standard deviation related to the square root of the number of events, $\sqrt{N}$.

A radiation source such as ^{192}Ir releases radiation randomly at a predictable average rate through radioactive decay. The process of radioactive decay depends on the number of parents which may decay, and a probability function which represents their natural lifetimes. The distribution of events resulting from radioactive decay follows a Gaussian or Poisson distribution, depending on the count rate [42]. Due to the random and independent nature of these events, given a number of events μ we can model

the decay using the Poisson distribution (Equation 5.13). The probability of x occurring is given by

$$P(x, \overline{x}) = \frac{\overline{x}^x}{x!} e^{-\overline{x}}. \tag{5.13}$$

For a large μ, the probability for a given x to occur is very nearly a Gaussian probability distribution function with mean μ and a standard deviation σ, which is conventionally used to quantify the uncertainty on a measurement sampled from the distribution. Given this behaviour of the Poisson distribution for a large number of events, we are able to apply counting statistics based on normal distributions in order to estimate the uncertainty associated with the distribution in question [42].

When using counting statistics, the standard deviation, σ_x, used to quantify the error, is defined as [43]

$$\sigma_x = \sqrt{\frac{1}{N} \sum_{i=1}^{N} (x_i - \overline{x})^2}, \tag{5.14}$$

where N is the number of measurements of a certain quantity. The standard deviation σ_x characterises the average uncertainty on each of the measurements.

5.4.2 Uncertainty on AAPM TG-43 parameters

In considering the uncertainty on the parameters output by the Geant4 simulation, the statistical uncertainty σ_x, as defined above, was considered. The statistical uncertainty on each energy measurement $E(r, \theta)$ was then calculated as $\sigma_{stat} = \sigma_x / E$. Additionally, the uncertainty on the cross-sections employed by Geant4, and the uncertainty on the photon emission spectrum, were considered. For these estimates, results from published works were employed.

The photon emission spectrum, σ_{I_γ}, consists of many individual spectral lines, each with a relative uncertainty. The uncertainty on the spectrum as a whole was calculated by Medich and Munro (2007) [33] as the intensity-weighted average of the uncertainty of each spectral line, and was found to be $\sigma_{I_\gamma} = 0.5\%$. This estimate is employed here.

Renner *et al* (2015) [44] calculated the uncertainty on the photon and electron cross-sections in Geant4. The uncertainty on the photon cross-sections is given as 0.43%, with the dominant contribution being uncertainty on the Compton scattering cross-section. The uncertainty on the electron cross-section was calculated to be 0.53%, yielding a total combined cross-section uncertainty of $\sigma_{x-sec} = 0.68\%$.

The percentage uncertainty on a measurement of a point with coordinates (r, θ) is given by

$$U_{P(r,\theta)} = \sqrt{\sigma_{stat}^2 + \sigma_{I_\gamma}^2 + \sigma_{x-sec}^2}, \tag{5.15}$$

such that the derived percentage uncertainties are then given by

$$U_{\dot{D}(r,\theta)} = \sqrt{\sigma_{stat}^2 + \sigma_{I_\gamma}^2 + \sigma_{x-sec}^2} \times \dot{D}(r, \theta), \tag{5.16}$$

and

$$U_{G_L(r,\theta)} = \sqrt{\sigma_{stat}^2 + \sigma_{I_\gamma}^2 + \sigma_{x-sec}^2} \times G_L(r,\theta). \tag{5.17}$$

In the case of the anisotropy function and radial dose function, the uncertainties can be estimated as

$$U_{F_L(r,\theta)} = \sqrt{(U_{\dot{D}(r,\theta)})^2 + (U_{\dot{D}(r,90^\circ)})^2 + (U_{G_L(r,90^\circ)})^2 + (U_{G_L(r,\theta)})^2} \tag{5.18}$$

and

$$U_g L(r) = \sqrt{(U_{\dot{D}(r,90^\circ)})^2 + (U_{G_L(1\ cm,90^\circ)})^2 + (U_{\dot{D}(1\ cm,\theta)})^2 + (U_{G_L(r,90^\circ)})^2}. \tag{5.19}$$

Chapter 6

Optimisation using the Harmony Search Algorithm

In high dose rate brachytherapy, as with any radiotherapy, an optimised treatment plan is essential in order to minimize the dose delivered to normal cells, and maximise the dose delivered to the tumour cells. This individualisation is facilitated by the use of mathematical optimisations done on the brachytherapy treatment plan through the manipulation of the dwell times.

In the case of this report, optimisation of the dose distribution will be performed in order to minimise dose to the organs at risk, while still achieving the desired dose to the tumour or cancerous lesions. This will be performed using the Harmony Search optimisation algorithm, a novel inverse planning-based optimisation technique which is not yet used at a clinical level in brachytherapy treatment for cervical cancer. The dose calculation employed during the optimisation algorithm is done using Monte Carlo techniques; the AAPM TG-43 dose calculation formalism is not used.

6.1 Optimisation

The dose to a point within the body is given by the sum of the doses to that point delivered by the source at each dwell point. In brachytherapy, optimisation of a dose distribution is the process of achieving desired dose values at points or within specified volumes, such as the target volume [45]. An optimised loading pattern leads to modification of spatial distribution of the dose. The optimisation is done by minimising the objective function, which is defined in terms of clinical objectives, limiting the minimum dose that the target can receive as well as the maximum dose that the organs at risk can receive. The objectives are related the the radiation doses; the dose domain defines the minimum underdose and the maximum overdose to the target, and the maximum overdose of the organs at risk.

A comprehensive review of all optimisation methods used for high dose rate brachytherapy was provided by Boeck *et al* (2011) [7], who state that, in general, optimisation methods used for this purpose are heuristic methods as they search by trial and error, and do not guarantee convergence. Heuristic optimisation methods can be stochastic, containing a probability or randomness aspect in their search process and coverging towards a global optimum, or deterministic, which have search processes which always execute in the same way.

Stochastic optimisation is chosen as the preferable algorithm, as its component of random sampling in the subspace of feasible solutions allows the optimisation to escape local minima should the converging function be trapped within one. The most widely used stochastic heuristic algorithm is named simulated annealing, and is based on the cooling process of metals during which the atoms move towards a perfect crystal structure. Also widely used are evolutionary algorithms, based on natural selection, which are capable of generating a wide range of optimal solutions [7].

A further algorithm, the Harmony Search optimisation method, is a stochastic optimisation method described in the review in its application to high dose rate brachytherapy for prostate cancer treatment in a paper by Panchal (2009) [46]. Based on the improvisation process of an orchestra, it combines elements of both simulated annealing and evolutionary algorithms, producing a novel optimisation technique which has successfully been applied to many real world problems [46]. A review of the literature of optimisation methods in cervical cancer brachytherapy treatment provides no evidence of the Harmony Search optimisation method having been used thus far.

6.1.1 Harmony Search Theory

The Harmony Search is a metaheuristic optimization algorithm [47]. It is an iterative process, improved by repetition, based on the harmony improvisation of an orchestra, where the best state is determined by audio aesthetic estimation; the most pleasing combination of pitches [46]. The harmony would be subject to objectives and constraints, as is the case in a brachytherapy treament plan. The aesthetic quality of a given note played by a musical instrument is determined by its pitch; that is, its frequency. The adjustment of a combination of pitches by an orchestra is the adjustment of their frequencies in order to achieve a pleasing harmony. While this harmony is subjective on the part of the listener to an extent, there are standard estimations to assess the nature of the harmony. For instance, frequency ratios are considered to be fundamental to the pleasantness of music. It was proposed by Helmholtz (1885) that the aesthetic quality of two simultaneous tones can be measured as a function of the ratio of their frequencies [48]. The combination of the ratios of each pair of notes, as well as the key of the harmony, constitute the objectives and constraints that are applicable in any optimisation problem.

The construction of a harmony may be undertaken in several ways; an orchestra may (1) play an existing piece from memory, (2) play something similar to a known piece with slight adjustments, or (3) play new and random notes [47]. These are the three components of the Harmony Search optimisation process. The optimisation is centred around the use of a Harmony Memory, defined as the set of vectors (which are combinations of pitches called harmonies, or, in the case of this problem, combinations of dwell times and dwell positions), which best satisfy the optimisation algorithm. Each vector represents the movement of the source through the applicator from beginning to end; it is the set of consecutive dwell points and their associated dwell times. The Harmony Memory is initially randomly constructed, but as the algorithm moves through iterations, the least satisfactory vectors are removed from the Harmony Memory and replaced with new and more efficient vectors. In this way, the Harmony Memory improves as the algorithm progresses. At the end of the optimisation, the optimal vector in the Harmony Memory is chosen as the optimisation outcome. The size, HMS, of the Harmony Memory is predetermined and sets a limit on how many harmonies can be saved as "good harmonies" at one time [7]. It is stored as an

$i \times j$ matrix, with $i = HMS$ vectors in the Harmony memory, each of length j.

The Harmony Search iteration begins with the production of a random number r between 0 and 1. This random number decides which of the three ways the new vector will be constructed. The Harmony Memory is assigned a parameter $r_{HM} \in [0, 1]$, defining the rate at which harmonies from the Harmony Memory are considered; that is, if the random number r is lower than r_{HM}, a vector from the Harmony Memory is selected as a starting point for the new vector. If the random number is higher than r_{HM}, a random vector is composed. It is suggested in the literature that a value of $r_{HM} \in [0.7, 0.95]$ is an optimal choice [47], since a good amount of harmonies are selected from memory, but the occasional exploration of random vectors (which can escape local minima) is allowed. In this report, $r_{\mathrm{HM}} = 0.9$. A vector chosen randomly from the Harmony memory and used with no adjustments is the equivalent of situation (1).

If a vector is chosen from memory, the pitch may be adjusted slightly as in situation (2). Whether the vector is adjusted is controlled by a pitch adjusting rate $r_{\mathrm{PA}} < r_{HM}$; that is, if the random number r is less than the pitch adjusting rate, the vector which has been selected from the Harmony Memory will also be adjusted slightly. In this case we employ a predetermined bandwidth bw and perform a linear adjustment of each element of the vector, such that [47]

$$x_i^{new} = x_i^{old} \pm bw * rand(0, 1). \tag{6.1}$$

It is suggested in the literature that an acceptable pitch adjustment rate is $r_{PA} < 0.5$. Here, $r_{PA} = 0.4$ has been used. The third situation, the randomization, occurs when the random number r is greater than r_{HM}. In this case, an entirely random new vector is composed. This is included to increase the diversity of the solutions and move towards a global solution, rather than a local one.

Once the new vector has been constructed, it is evaluated using the objective function, as are the vectors in the Harmony Memory. If the new vector is 'better' than the 'worst' member of the Harmony Memory, that is, if it fulfils the conditions of the objective function better, then the new vector replaces the old member of the Harmony Memory. The pseudocode is given in Algorithm 1, including the Harmony Memory initialization and new vector construction. The vectors x, both those in the Harmony Memory and those which are newly generated, are evaluated using the objective function, indicated by $f(x)$ in the pseudocode. The objective function represents the desired dose to the target volume, and the constraints on dose to the organs at risk. The constraints divide the solution subspace into feasible and infeasible solutions.

As the optimisation progresses through iterations, the number of *different* harmonies saved in the Harmony Memory decrease, as the vectors which do not satisfy the objective function are replaced with those that do. However, the number of vectors remains constant at all times (although there will be multiple copies of the same vector as the iterations progress). Note that, if $r_{PA} < r < r_{HM}$, the new vector will be an identical copy of one of the vectors, v_i, already contained in the Harmony Memory. If this new vector satisfies the objective function better than one of the vectors, v_j, in the Harmony Memory, it will replace that vector, and there will be two copies of the same vector v_i in the Harmony Memory. In this way, the function converges to a global minimum, as all of the vectors in the Harmony Memory move towards the optimal result. This global minimum is the most effective treatment plan

Algorithm 1: Harmony Search Pseudocode

```
   /* Harmony Memory initialization                                    */
1  for i = 0, i < HMS do
2  |  for j = 0, j < vector length do
3  |  |  x_ij = rand(0,1) × DT_max
4  |  end
5  end
   /* New vector construction                                          */
6  r = rand(0,1)
7  HM member x = (int)rand[1,5]
8  for j = 0, j < vector length do
9  |  if r < r_HM then
10 |  |  x_j = x_j
11 |  |  if r < r_PA then
12 |  |  |  x_j = x_j + rand[−1,1]bw
13 |  |  end
14 |  end
15 |  else
16 |  |  x_j = rand(0,1) × DT_max
17 |  end
18 end
   /* Evaluate the new candidate                                       */
19 if f(x_new) better than f(x_HM^worst) then
20 |  Replace x_HM^worst with x_new
21 end
22 else
23 |  Disregard x_new
24 end
25 endif Optimisation condition is met
```

resulting in the optimal dose distribution, and represents the most pleasing harmony.

6.1.2 The Objective Function

The objective function serves to ensure that a lethal dose is delivered to the target, while the dose to the surrounding organs at risk is limited. It translates these goals and constraints into mathematical functions. We can write that, for an HDR brachytherapy source moving through a number of dwell points, the total dose to point i is given by $\sum_j \dot{d}_{ij} t_j$, where $\dot{d}_{ij}$ is the dose rate contribution at point i from a source at point j, and $t_j \geq 0$ is the time spent by the source at point j [49]. The typical high dose rate brachytherapy optimisation problem is defined in terms of a multicriteria approach, where the single objective function is a weighted sum of different objectives. The weights denote the importance of the objectives, although the optimal values of the weights are not known [7]. In this optimisation, a multicriteria approach will be employed.

It is assumed, in the following, that upper and lower dose limits have been stipulated for each organ which is to be considered, with incentives applied to find solutions within the limits. Weights are used not only to reward solutions which follow the constraints, but also to penalise those which violate the constraints. In the following, the model uses a weighted sum to define a single objective problem, which for a set of structures S is of the form [49]

$$\min \sum_{s \in S} \left(w^s_{min}(\underline{\Delta}_s) + w^s_{max}(\overline{\Delta}_s) \right). \tag{6.2}$$

Here, $w^s_{min(max)}$ is the weight for under(over)dosage of a given structure s. We also define $\underline{\Delta}_s = L^s_{min} - D^s_i$ and $\overline{\Delta}_s = D^s_i - L^s_{max}$, where $L^s_{min(max)}$ is the lower(upper) dose limit for structure s, and $D^s_i = \sum_{j \in T} \dot{d}^s_{ij} t_j$ is the total dose to calculation point i in structure s . The weights $w^s_{min(max)}$ can be understood as a penalty for underdosing or overdosing a structure; the more important the limit, the higher the weight.

It is clear from the structure of a function that the lower the value that the objective function returns, the better the dose distribution would be. For example, in the case of an organ at risk to which the dose may not exceed the maximum tolerable limit, $D^s_i - L^s_{max} \in [-L^s_{max}, 0]$, and so the further the dose is from the maximum tolerable dose, the more $D^s_i - L^s_{max}$ tends to the lower limit. If the dose exceeds the maximum tolerable limit, the term becomes greater than 0, and moves further away from the lower limit. Similarly, in considering the dose to a target structure, to which the dose should be maximised $L^s_{min} - D^s_i \in [L^s_{min} - D^s_i, L^s_{min}]$, and so the higher the dose, the more the term tends to its lower limit. The goal of the optimisation algorithm is then to find the set of solutions for which the objective function is minimized.

6.2 Implementation of the Harmony Search

The Harmony Search optimisation was performed on a GammaMed source moving through an applicator as would occur in a clinical setting at CMJAH. In order to do this, applicators whose dimensions and materials correspond to those used at CMJAH were simulated to be at the centre of a spherical water phantom of 2 m diameter, which can be considered semi-infinite. The simulation of the applicators is

described in Section 6.2.1. The optimisation itself, including the code which was designed in this report to execute it as well as the parameters chosen, is described in Section 6.2.2. The results of the optimisation are given in Section 6.2.3.

6.2.1 Applicators

The tandem and ring applicator system described in Section 3.3 was simulated in order to perform an optimisation of a typical brachytherapy treatment. A diagram of the system is shown in Figure 6.1, including the angles of the ring applicator and the intrauterine tandem applicator. The parallel rods of the applicator lie along the z-axis in the same y-plane.

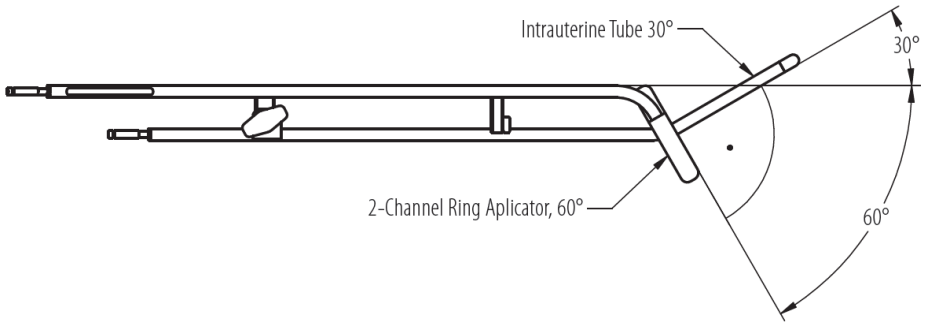


FIGURE 6.1: Diagram of a tandem and ring applicator as simulated in this report [20].

The metal rods of the applicator were simulated as titanium metal, with density 4.50 g/cm^3, with an outer radius of 3 mm. A cylinder of air with outer radius 1.5 mm was placed within the metal rods, as the applicators must have a hollow centre to allow the source to pass through them. The density of the air was nominated as $\rho = 1.290$ mg/cm^3. The tandem, or intrauterine applicator, was positioned at an angle of 30° to the nominal z-axis, and has a length of 60 mm. The ring applicator is simulated as having the same hollow titanium composition as the rods, with an additional outer layer of plastic (acetal), which is simulated to have a density of $\rho = 1.41$ g/cm^3. This plastic ring has an outer radius of 7.5 mm, measured from the midpoint of the air cavity within the ring, and encases the titanium ring through which the source travels. The ring is orientated at an angle of -60° to the nominal z-axis. The simulated applicator system is shown in Figure 6.2, where the titanium rods are depicted in blue, and the plastic ring is depicted in green.

6.2.2 Optimisation specifics

In order to perform an optimisation, 11 dwell positions were specified; four positions were defined at equal spacings around the ring, and seven positions were defined with 10 mm spacings along the intrauterine applicator. The positions are depicted in Figure 6.2. The source was simulated to move first around the ring in a clockwise direction around the z-axis, and then up the intrauterine applicator. The movement of the source between dwell points was not taken into account; the source was simply simulated at each successive dwell position.

The dose was measured in Gray (Gy) at two positions, intended to represent Point A and an organ at risk. In order to measure the dose, two scoring volumes were defined with dimensions

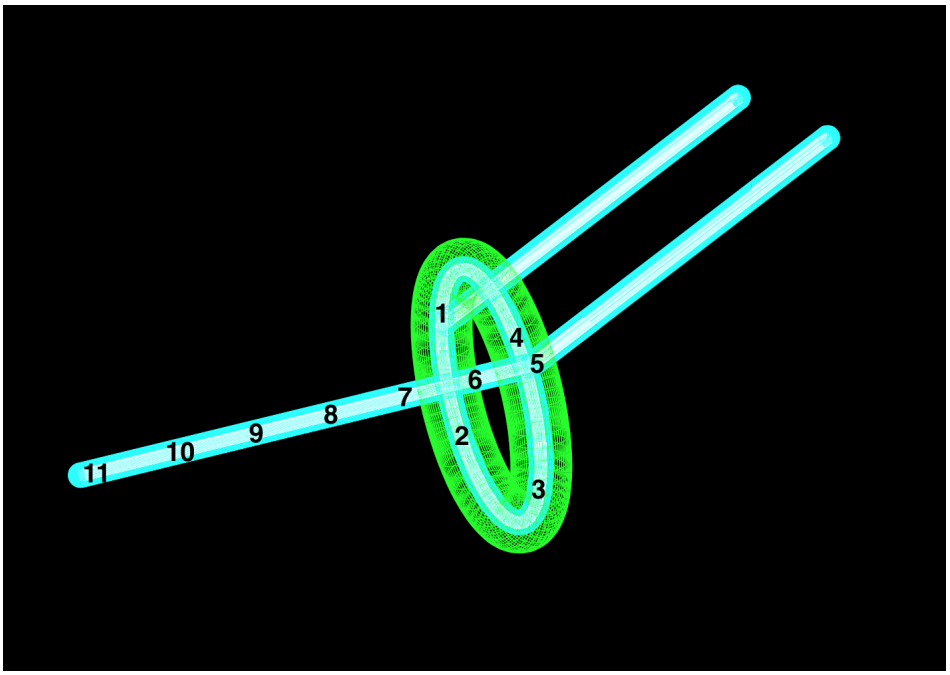


FIGURE 6.2: Tandem and ring applicator as simulated using Geant4. The dwell points for the optimisation are numbered 1-11.

$10 \times 0.25 \times 10$ mm^3, as the applicator system lies in the $x - z$ plane. The first of the scoring volumes, intended to denote Point A, is positioned at (0 cm, 2 cm, 2 cm), from the centre of the ring, in accordance with the ICRU 38 guidelines. The second of the scoring volumes is placed at (-1 cm, -3 cm, 0 cm), and is intended to denote an organ at risk. Given that, in a clinical setting, the positions of the organs at risk are measured in each patient, a random coordinate was used here.

In order to perform the optimisation, the following steps were performed using a combination of ROOT version 5.34/36 and Geant4, all written in C++. ROOT [50] is a software framework developed at CERN in Geneva, which is designed for data analysis and visualisation. The optimisation code here is run using ROOT. The optimisation relies on the use of random numbers generated by C++; however, as a computer cannot perform a truly random generation, the generator is in fact pseudorandom. The random number generator employed by C++ uses the time at which the program is run as an ever-changing input, and outputs a pseudorandom number.

Due to the sheer number of decays associated to a second of dwell time, the number of decays associated to a second that was determined during the calibration was not employed for the purposes of the optimisation. Instead, 100000 events were assigned to represent one second of dwell time. This was to ensure that the optimisation was run in a reasonable amount of time on the low power personal computer that was used for this simulation. With this new assignment of number of events to second, it nonetheless took up to four hours to simulate each of the vectors in the harmony memory with each iteration. It should then be noted that there is a large uncertainty associated with these dose measurements, but the principle of the optimisation remains the same.

Before the simulation, the starting point for the optimisation was determined by measuring the total dose to the two scoring meshes, referred to below as point A and the organ at risk, for a treatment plan

during which the source remained at each dwell point for the maximum dwell time, which was set as 100 s. The dose delivered to point A was measured to be 3.57 Gy, and the dose to the organ at risk was measured to be 1.65 Gy. For a treatment plan where the source remained at each dwell point for 50 s, a dose of 1.65 Gy was delivered to Point A, and a dose of 1.02 Gy delivered to the organ at risk. This was used to assign dose constraints.

The bounds set on the simulation, including maximum and minimum doses and associated weights, are displayed in Table 6.1. The weights are chosen according to the strictness of the limit. In this treatment, the delivery of the minimum acceptable dose (here set to 2.5 Gy) is set to be the most important weight, given that the success of a treatment depends on the delivery of the minimum dose to the target. Given that a goal of radiotherapy is the delivery of the maximum possible dose to the target while managing the dose to the normal tissues, the optimisation is set up such that the target should receive at least its minimum acceptable dose, but vectors which are able to deliver a higher dose to the target while still respecting the maximum dose to the organ at risk will be preferred. The goal is then to maximise the dose to the target, provided it does not exceed its maximum tolerable dose, which could cause organ failure in a clinical setting. The second most important weight is the maximum tolerable dose to the organ at risk, here set to be 1.5 Gy. The final constraint, the maximum dose to the target, is the least important constraint, set to be 4.0 Gy.

Structure	Dose Limit	Weight
Point A	D_{min} = 2.5 Gy	4
	D_{max} = 4.0 Gy	1
OAR	D_{max} = 1.5 Gy	3

TABLE 6.1: Constraints set for the optimisation.

The optimisation was then run. First, the Harmony memory was initialised by randomly choosing 5 vectors of 11 dwell times, each corresponding to a dwell point. This was performed by the generation of random numbers $r \in (0, 1)$, which were multiplied by the maximum dwell time. The Harmony Memory at initialisation is given in Table 6.2. The Harmony Memory was stored as a 5×11 matrix. The Harmony Memory vectors were then output into a Geant4 macro file, which defined the dwell points and corresponding dwell times for each of the Harmony Memory vectors. These macro files were fed into Geant4, and used to simulate the source moving through the applicator according to each vector in the Harmony Memory. For each of the five vectors in the Harmony memory, the energy depositions to each of the scoring meshes were saved.

Following this, a new vector was generated. The Harmony Memory Considering Rate was set to 0.9, the Pitch Adjusting Rate to 0.4, and the bandwidth to 10 s. First, a random number $r_1 \in (0, 1)$ was generated, and a member of the existing Harmony Memory randomly picked. The steps described in Section 6.1.1 were then followed in order to construct a new vector. The new vector was then used by Geant4 to simulate a source moving through the applicator, and the energy depositions to the scoring regions were saved.

The doses to each scoring region due to each of the Harmony Memory vectors and the new vector was evaluated according to the objective function $f(d_{ptA}, d_{OAR})$ defined in Equation 6.3 according to the theory in Section 6.1.2,

$$f(d_{ptA}, d_{OAR}) = w_{min,ptA}(D_{min,ptA} - d_{ptA}) + w_{max,ptA}(d_{ptA} - D_{max,ptA}) + w_{max,OAR}(d_{OAR} - D_{max,OAR}), \tag{6.3}$$

where $d_{ptA(OAR)}$ is the dose calculated by the simulation to the scoring volume representing Point A (the organ at risk), and $D_{min(max),ptA(OAR)}$ is the minimum(maximum) allowed dose to the relevant structure. The objective function is defined in order to minimize average dose to critical structure, and maximise dose to target structure. There is a minimum and a maximum dose defined for the target. If the new vector yielded a score better than or equal to the worst score in the Harmony Memory, it was kept, and the worst Harmony Memory score discarded.

6.2.3 Optimisation results

The optimisation was allowed to run for one week, which amounted to 40 iterations. Initially, 5 random vectors were selected, shown in Table 6.2, the most suitable of which was vector 3 with an objective function score of -2.69. This vector yielded a dose to the target of 2.46 Gy, and a dose to the critical structure of 1.06 Gy. The first random iteration yielded a vector $v_{it,\,1}$ with a score of -2.73, with a dose to the target of 2.59 Gy and a dose to the critical structure of 1.18 Gy. While this plan yielded a higher dose to the organ at risk, it was still below the maximum tolerable dose, and delivered the required minimum dose to the target.

In the 22nd iteration, a vector $v_{it,\,22}$ was produced from a pitch adjustment of $v_{it,\,1}$, yielding a score $f(v_{it,\,22})$ = -3.51, with a dose to the target of 2.93 Gy and a dose to the critical structure of 1.23 Gy. The 32nd iteration produced a vector $f(v_{it,\,32})$ = -3.66, through a pitch adjustment of $v_{it,\,22}$, with a dose to the target of 3.03 Gy and a dose to the critical structure of 1.31 Gy. This vector was the optimal vector produced during the optimisation. The algorithm produced a random vector 5 times during the 40 iterations, underwent 20 pitch adjustments, and 15 comparisons using an existing Harmony Memory vector. The vectors produced during the iterations are given in Tables 6.3 and 6.4.

At the termination of the optimisation, the Harmony Memory, shown in Table 6.5, consisted of only two different vectors, both of which satisfied the constraints. The vector with the lower score was considered to be the preferred candidate. The optimal plan was that which had an objective function score of $f(v) = -3.66$, delivering a sufficient dose to the target while remaining well below the maximum tolerable dose to the organ at risk.

Vector x	Components (s)											D(Pt A)	D(OAR)	Score $f(x)$
1	93.34	23.88	11.49	6.43	34.15	62.00	89.79	24.36	94.60	1.85	64.13	2.24	1.01	-2.19
2	80.12	56.66	6.31	73.34	42.41	39.09	70.69	30.26	30.06	62.44	28.59	1.11	0.78	0.5
3	50.230	69.79	23.05	87.85	78.43	15.60	16.37	79.26	1.13	34.26	53.26	2.46	1.06	-2.69
4	95.82	87.99	76.62	77.10	72.74	79.02	75.64	27.76	62.15	73.59	45.71	1.83	1.06	-0.811
5	99.51	94.40	19.01	70.43	6.95	66.51	20.13	86.69	56.26	33.56	73.55	2.83	1.59	-2.20

TABLE 6.2: Harmony Memory vectors at the initialisation of the simulation.

Iteration	Random Number	New Vector Components (s)											Score $f(x)$	Kept?
1.	0.93	64.85	81.62	53.81	93.38	18.01	31.68	2.18	62.67	94.23	91.77	55.24	-2.73	Yes
2.	0.38	91.95	97.75	74.61	77.38	65.94	84.20	79.47	18.54	55.39	78.97	39.23	-2.65	Yes
3.	0.91	19.05	71.34	91.48	18.71	23.12	8.45	64.49	23.89	74.40	70.72	63.42	-2.58	Yes
4.	0.56	64.85	81.62	53.81	93.38	18.01	31.68	2.18	62.67	94.23	91.77	55.24	-2.73	Yes
5.	0.57	19.05	71.34	91.48	18.71	23.12	8.45	64.49	23.89	74.40	70.72	63.42	-2.58	No
6.	0.69	64.85	81.62	53.81	93.38	18.01	31.68	2.18	62.67	94.23	91.77	55.24	-2.73	Yes
7.	0.26	70.17	73.99	59.27	95.21	22.35	30.94	4.39	60.56	95.19	97.23	46.56	-1.64	No
8.	0.36	100.00	96.40	72.71	81.54	68.60	75.55	87.89	19.81	57.31	85.09	36.42	-2.13	No
9.	0.87	64.85	81.62	53.81	93.38	18.01	31.68	2.18	62.67	94.23	91.77	55.24	-2.73	Yes
10.	0.22	66.13	77.00	44.65	87.35	27.79	40.79	4.85	62.40	93.02	94.36	53.76	-2.57	No
11.	0.57	50.30	69.79	23.05	87.85	78.43	15.60	16.37	79.26	1.13	34.26	53.26	-2.69	No
12.	0.11	55.86	80.88	49.70	88.37	19.94	31.12	9.21	69.57	101.25	82.34	63.36	-2.16	No
13	0.78	64.85	81.62	53.81	93.38	18.01	31.68	2.18	62.67	94.23	91.77	55.24	-2.73	Yes
14	0.25	65.68	78.94	57.15	100.07	12.96	28.25	3.53	68.18	89.88	81.83	48.15	-1.59	No
15	0.95	22.45	95.11	19.75	97.48	28.86	65.92	50.88	81.63	77.04	21.62	1.61	1.46	No
16	0.12	61.98	73.35	47.93	86.62	25.36	26.01	10.19	70.71	87.97	88.95	48.06	-0.87	No
17	0.70	64.85	81.62	53.81	93.38	18.01	31.68	2.18	62.67	94.23	91.77	55.24	-2.73	Yes
18	0.02	56.99	87.06	59.91	91.85	25.20	30.61	5.28	56.42	88.55	85.92	48.10	-2.22	No
19	0.20	69.21	85.00	46.84	93.44	11.29	31.79	5.10	68.05	92.36	98.83	48.55	-1.86	No
20	0.88	64.85	81.62	53.81	93.38	18.01	31.68	2.18	62.67	94.23	91.77	55.24	-2.73	Yes

TABLE 6.3: Vectors initialised during the iterations.

Iteration	Random Number	New Vector Components (s)											Score $f(x)$	Kept?
21	0.31	72.25	91.51	53.17	90.57	23.74	22.68	3.28	71.80	88.87	100.34	54.44	-2.30	No
22	0.37	63.92	83.17	55.91	100.13	11.55	31.52	4.40	63.62	88.20	94.88	61.32	-3.51	Yes
23	0.70	64.85	81.62	53.81	93.38	18.01	31.68	2.18	62.67	94.23	91.77	55.24	-2.73	Yes
24	0.41	63.92	83.17	55.91	100.13	11.55	31.52	4.40	63.62	88.20	94.88	61.32	-3.51	Yes
25	0.12	69.57	71.70	47.43	90.04	27.60	27.61	1.76	65.13	97.48	94.42	56.03	-2.47	No
26	0.79	64.85	81.62	53.81	93.38	18.01	31.68	2.18	62.67	94.23	91.77	55.24	-2.73	Yes
27	0.08	65.54	91.43	63.58	102.48	11.80	25.04	11.18	69.74	86.36	97.08	61.62	-3.42	Yes
28	0.89	63.92	83.17	55.91	100.13	11.55	31.52	4.40	63.62	88.20	94.88	61.32	-3.51	Yes
29	0.68	65.54	91.43	63.58	102.48	11.80	25.04	11.18	69.74	86.36	97.08	61.62	-3.42	Yes
30	0.92	6.55	20.54	79.31	71.22	18.53	23.46	55.25	26.02	37.99	12.09	20.62	1.19	No
31	0.39	56.81	81.62	67.71	97.63	17.00	24.28	20.79	69.58	78.57	89.81	52.44	-2.13	No
32	0.05	66.13	75.18	49.22	96.00	21.23	33.00	12.85	59.33	87.37	102.40	61.99	-3.66	Yes
33	0.30	68.90	84.38	55.92	109.42	9.47	22.26	5.42	72.72	86.63	102.90	62.51	-3.49	Yes
34	0.41	66.13	75.18	49.22	96.00	21.23	33.00	12.85	59.33	87.37	102.40	61.99	-3.66	Yes
35	0.28	60.43	79.05	39.60	88.73	26.68	26.56	10.27	60.69	78.33	99.04	52.79	-1.69	No
36	0.56	63.92	83.17	55.91	100.13	11.55	31.52	4.40	63.62	88.20	94.88	61.32	-3.51	Yes
37	0.34	62.37	69.55	40.36	97.53	14.98	34.88	18.92	66.70	88.28	93.74	53.68	-2.23	No
38	0.98	20.24	88.12	95.96	40.08	36.65	83.20	6.28	48.31	48.27	36.09	39.37	0.38	No
39	0.08	54.98	88.82	53.41	106.68	10.79	22.50	11.68	64.40	80.42	89.07	65.38	-2.23	No
40	0.23	62.26	90.30	53.98	90.67	15.10	29.19	13.31	68.16	92.94	104.88	55.79	-3.32	No

TABLE 6.4: Vectors initialised during the iterations (continued).

Vector x	Components (s)											D(Pt A)	D(OAR)	Score $f(x)$
1	63.92	83.17	55.91	100.13	11.55	31.52	4.40	63.62	88.20	94.88	61.32	2.93 Gy	1.23 Gy	-3.51
2	63.92	83.17	55.91	100.13	11.55	31.52	4.40	63.62	88.20	94.88	61.32	2.93 Gy	1.23 Gy	-3.51
3	63.92	83.17	55.91	100.13	11.55	31.52	4.40	63.62	88.20	94.88	61.32	2.93 Gy	1.23 Gy	-3.51
4	66.13	75.18	49.22	96.00	21.23	33.00	12.85	59.33	87.37	102.40	61.99	3.03 Gy	1.31 Gy	-3.66
5	66.13	75.18	49.22	96.00	21.23	33.00	12.85	59.33	87.37	102.40	61.99	3.03 Gy	1.31 Gy	-3.66

TABLE 6.5: Harmony Memory vectors at the conclusion of the simulation.

Chapter 7

Application to Future Research

The work done in this report may be extended in further research in many ways. In this chapter, suggestions are made as to paths of future research which may build from this report. These suggestions include the use of imaging modalities to include real patient tissue properties in the Monte Carlo simulation, optimisation of the position of the applicators, and inclusion of the transit dose in calculations.

At CMJAH, treatment planning and reporting is done using CT scans of the patient. These images are maps of the attenuation coefficients of the tissues of the body, which are directly proportional to the density of those tissues. CT scans can then provide valuable information on the detailed anatomy of the patient, including tissue inhomogeneities and precise information about the location of the cancerous lesions and the organs at risk, and can be used to precisely plan brachytherapy treatements. However, treatment planning using the AAPM TG-43 protocol simply uses these scans to mark the position of the critical structures, and simulates the body as being composed of water. The capability exists in Monte Carlo simulation to use these CT scans, or other imaging modalities, to take account of the variations in tissue within the body and to calculate a dose distribution which is more specified to the patient. The simulations in this report were done in this report by simulating the source to sit within a water phantom. While this is instructive as it mimics the conditions laid out in the AAPM TG-43 protocol, an interesting extension of this research would be to use real patient data in the Monte Carlo simulation in order to take account of variations in tissue composition, and assess the impact that this has on the dose distribution. It could be an interesting application of further research to compare this dose distribution, modelled using real patient tissue attenuation, with a dose distribution calculated using the AAPM TG-43 formalism.

In a case where patient data is included by way of images, the position of the catheters may also be optimised for the treatment plan in order to find the most efficient dose distribution [49]. This, in combination with an optimisation of the dwell times, may further improve the sparing of the organs at risk while accurately targeting the cancerous lesion.

In this report, the transit dose, which is the absorbed dose that may be imparted to surrounding tissues while the source moves from housing to the applicator and between dwell points, is not considered. The source is simply simulated to appear at each of the consecutive dwell points; it is not simulated to travel between the points as would occur in a clinical situation. This transit dose is also usually disregarded in treatment planning systems [15]. However, in cases of future research in this topic, it would be instructive to include the transit of the source in the simulation, in order to assess the magnitude of the transit dose.

Chapter 8

Conclusion

In this report, an optimisation using the Harmony Search algorithm has been done, and the AAPM TG-43 parameters have been reproduced. The parameters, in general, agreed with published data within uncertainty. In particular, the agreement of the geometry function with published data was excellent. There was some statistical fluctuation visible in the calculation of the anisotropy function, given that this function relies on the dose and not simply the geometry of the setup. The radial dose function agrees fairly well with published data. It is possible that, with greater computing power, these simulations could be run for larger data sets and this statistical fluctuation could be lessened.

An advantage of using Monte Carlo simulations to calculate the absorbed dose is that no assumptions need to be made. In this report, no simplifications regarding the scatter from source shielding or the shape of the source were made. Indeed, the transit dose was neglected in the simulation as it would be in a conventional treatment planning system, but it need not be the case. As mentioned in the previous section, the body need not be approximated as water when using a Monte Carlo simulation. For these reasons and many others, Monte Carlo simulations are a powerful tool in medical physics.

As the treatment planning done in brachytherapy for cervical cancer continues to develop in complexity around the world, higher resource centres are moving towards Monte Carlo-based treatment planning programmes, which not only calculate the dose to critical structures using Monte Carlo methods, but also perform optimisations on the treatment plan to find the most efficient plan possible. However, in a clinical context, especially in a centre such as CMJAH in which there is a high volume of patients, it is imperative that the optimisation be performed in a reasonable amount of time. Many Monte Carlo simulations, including Geant4, demand a large amount of computing power. This is apparent in the time it took to run the optimisation in this report. The demand for Monte Carlo systems to be used for clinical dose calculations has spurred the introduction of many 'fast' Monte Carlo systems able to perform dose calculations in one minute [51]; it is clear, then, that Geant4 is not one of these. Perhaps with a faster and more capable computer, the processing time of a Geant4 dose calculation could be reduced, but it is unlikely to approach the realms of one minute.

However, this limitation is due to Geant4, not the Harmony Search optimisation algorithm. The optimisation algorithm, although slow due to computational limitations, was able to calculate the most efficient treatment plan which satisfied the constraints and optimisations well. In observing the step by step progression of the optimisation, its strengths are clear. The algorithm began with five random vectors, and within the first few iterations had quickly weeded out those which were severely unsatisfactory. In fact, the first new vector, referred to as $v_{it,\,1}$, composed by randomisation satisfied all

the constraints, with a dose to the target of 2.59 Gy and a dose to the critical structure of 1.18 Gy, and an objective function score of $f(x) = -2.73$. The algorithm then continued to run, composing new vectors and comparing vectors within the Harmony Memory against each other, until there were multiple instances of $v_{it,\,1}$, which remained the 'best' vector, within the Harmony Memory. This meant that, statistically, it was more probable that $v_{it,\,1}$ would be selected as the new vector, and a pitch adjustment on this vector may yield an even better fit. Pitch adjustments on $v_{it,\,1}$ returned worse fits, until iteration 22, which yielded a vector $v_{it,\,22}$ with a dose to the target of 2.93 Gy and a dose to the critical structure of 1.23 Gy, and an objective function score of $f(x) = -3.51$. Although this vector returns a higher dose to the organ at risk, the dose is still within the maximum tolerable dose, and the dose to the target is higher. Given that the weight assigned to delivering a high dose to the tumour was the highest of the weights, maximising the dose to the tumour is the most important objective, and this vector returned a better score. A further pitch adjustment on this vector yielded the optimal outcome of the optimisation, $f(v_{it,\,32}) = -3.66$, with a dose to the target of 3.03 Gy and a dose to the critical structure of 1.31 Gy.

It is apparent that the pitch adjustment component of the optimisation algorithm is critical to the success of the method; the optimal vector was produced via two successive pitch adjustments of a randomly produced vector. A reader can imagine an orchestra making small adjustments to an already pleasant harmony or melody in order to achieve an even better sound; the usefulness of this method in an optimisation context is clear.

It is apparent also that the choice of the weights by the physicist is of paramount importance to the outcome of the optimisation, as it influences the scores heavily. As stated by Boeck *et al* (2011) [7], the physicist does not know ahead of time what the optimal solution of the weights are - one can only assign weights which are deemed appropriate to the importance of the limit, and it is clear that different patients may require different weights, based on their individual circumstance.

During this optimisation, the simulation of each vector took approximately 4 hours, although the simulation did conclude having produced a plan which fits all constraints posed. This is clearly not useful in a clinical context, and particularly at CMJAH, where the volume of patients would not allow for a week-long treatment planing optimisation per patient. However, with another Monte Carlo program which may be quicker to perform this simulation, such as the fast Monte Carlo toolkits mentioned above, the Harmony Search algorithm may prove a useful tool.

As treatment planning of brachytherapy for cervical cancer begins to move towards Monte Carlo simulations, it is instructive to continue to compare older methods such as the AAPM TG-43 formalism with the newer planning systems. Patients undergoing radiotherapy should receive the best possible treatment planning, to ensure an efficient and successful treatment with minimal side effects. The investigation into Monte Carlo methods which could one day replace the AAPM TG-43 formalism should continue, and with it, the assessment of optimisation algorithms which enable the best possible treatment plan to be devised. The Harmony Search algorithm has been shown to be an innovative and useful algorithm, and with greater computing power has the potential to form part of a successful treatment planning programme for high dose rate brachytherapy for cervical cancer.

Bibliography

[1] Kari Tanderup et al. “Curative Radiation Therapy for Locally Advanced Cervical Cancer: Brachytherapy Is NOT Optional”. In: *International journal of radiation oncology, biology, physics* 88 (Jan. 2014).

[2] F.B Atkins and D Van Nostrand. “Simplified Methods of Dosimetry”. In: *Thyroid Cancer: A Comprehensive Guide to Clinical Management (3rd Edition)*. Ed. by L. Wartofsky and D. Van Nostrand. Springer, 2016. Chap. 59.

[3] Ram Abhinav Kannan et al. “Comparison of manual and inverse optimisation techniques in high dose rate intracavitary brachytherapy of cervical cancer: A dosimetric study”. In: *Reports of Practical Oncology & Radiotherapy* 20 (June 2015).

[4] M.J Rivard et al. “Update of AAPM Task Group No. 43 Report: A revised AAPM protocol for brachytherapy dose calculations”. In: *Med. Phys.* 31(3) (2004).

[5] D. W. O. Rogers and A. F. Bielajew. “Monte Carlo Techniques of Electron and Photon Transport for Radiation Dosimetry”. In: *The Dosimetry of Ionizing Radiation (III)*. Ed. by K. R. Kase and B. E. Bjarngard. Academic Press, 2014. Chap. 5.

[6] S. Agostinelli et al. “GEANT4: A Simulation toolkit”. In: *Nucl. Instrum. Meth.* A506 (2003), pp. 250–303. DOI: 10.1016/S0168-9002(03)01368-8.

[7] L. De Boeck, J. Beliën, and W. Egyed. “Dose optimization in high-dose-rate brachytherapy: A literature review of quantitative models from 1990 to 2010”. In: *Operations Research for Health Care* 3(2) (2014). doi:10.1016/j.orhc.2013.12.004, pp. 80 –90. ISSN: 2211-6923. URL: http://www.sciencedirect.com/science/article/pii/S2211692313000428.

[8] E.B. Podgorsak. *Radiation Oncology Physics: A Handbook for Teachers and Students*. Vienna: International Atomic Energy Agency, 2005.

[9] J.V Siebers and G.D Hugo. “Basic Radiation Interactions, Definition of Dosimetric Quantities, and Data Sources”. In: *Clinical Dosimetry Measurements in Radiotherapy (2009 AAPM Summer School)*. Ed. by D.W.O. Rogers and J.E Cygler. Medical Physics Publishing, 2009. Chap. 2, pp. 30–86.

[10] David J. Thomas. “ICRU report 85: fundamental quantities and units for ionizing radiation”. In: *Radiation Protection Dosimetry* 150(4) (2012). doi:10.1093/rpd/ncs077, pp. 550–552. eprint: /oup/backfile/content_public/journal/rpd/150/4/10.1093/rpd/ncs077/2/ncs077.pdf. URL: +http://dx.doi.org/10.1093/rpd/ncs077.

[11] INTERNATIONAL ATOMIC ENERGY AGENCY. *Management of Cervical Cancer: Strategies for Limited-resource Centres - A Guide for Radiation Oncologists*. Vol. 6. IAEA Human Health Reports. Vienna: INTERNATIONAL ATOMIC ENERGY AGENCY, 2013. URL: http://www-pub.iaea.org/books/IAEABooks/8738/Management-of-Cervical-

Cancer-Strategies-for-Limited-resource-Centres-A-Guide-for-Radiation-Oncologists.

[12] E. Browne. *Table de Radionucleides:* ^{192}Ir. BNM - CEA/LNHB. 2003. URL: http://www.nucleide.org/DDEP_WG/Nuclides/Ir-192_tables.pdf.

[13] KÃ¡tia A. Fonseca, Marina F. Koskinas, and Mauro S. Dias. "Disintegration rate measurement of a 192Ir solution". In: *Applied Radiation and Isotopes* 54.1 (2001), pp. 141 –145. ISSN: 0969-8043. DOI: https://doi.org/10.1016/S0969-8043(00)00158-5. URL: http://www.sciencedirect.com/science/article/pii/S0969804300001585.

[14] Michael C. Joiner and Albert van der Kogel. *Basic Clinical Radiobiology Fourth Edition*. eng. 4th ed. CRC Press, 2009. URL: https://www.123library.org/ebook/isbn/9781444109610/.

[15] J Venselaar and J (eds.) Pérez-Calatayud. "ESTRO Booklet No. 8: A practical guide to quality control of brachytherapy equipment". In: *European guidelines for quality assurance in radiotherapy* (2004).

[16] Robyn Banerjee and Mitchell Kamrava. "Brachytherapy in the treatment of cervical cancer: A review". In: *International journal of women's health* 6 (May 2014), pp. 555–564.

[17] JJ. Mazeron et al. "Radiobiology of Brachytherapy and the Dose-Rate Effect". In: *The GEC ESTRO Handbook of Brachytherapy*. Ed. by A. Gerbaulet et al. ACCO, 2002. Chap. 4, pp. 95–121.

[18] L Bruni et al. "Human Papillomavirus and Related Diseases Report". In: *ICO/IARC Information Centre on HPV and Cancer (HPV Information Centre)* (2017). Date Accessed: 06 March 2018.

[19] J.N.W. Lim and A.A. Ojo. "Barriers to utilisation of cervical cancer screening in Sub Sahara Africa: a systematic review". In: *European Journal of Cancer Care* 26(1) (2016).

[20] Nucletron: An Elektra Company. *Brachytherapy applicators and accessories: An Applicator Guide*. 2016. URL: https://www.elekta.com/brachytherapy/.

[21] "Dosimetry of interstitial brachytherapy sources: Recommendations of the AAPM Rdiation Therapy Committee Task Group No. 43". In: ().

[22] ICRU. "Dose and volume specification for reporting intracavitary brachytherapy in Gynaecology ICRU Report No. 38". In: *International Commission on Radiation Units and Measurements ICRU* (1985).

[23] A. Allisy et al. "Report 60". In: *Journal of the International Commission on Radiation Units and Measurements* os31.1 (1998), NP. DOI: 10.1093/jicru/os31.1.Report60. eprint: /oup/backfile/content_public/journal/jicru/os31/1/10.1093_jicru_os31.1.report60/2/jicruos31-np.pdf. URL: http://dx.doi.org/10.1093/jicru/os31.1.Report60.

[24] H Zaidi. "Monte Carlo techniques in diagnostic and therapeutic nuclear medicine". In: *International Atomic Energy Agency (IAEA)* IAEA-CN–96 (2002).

[25] L. Archambault et al. "Overview of Geant4 applications in medical physics". In: *2003 IEEE Nuclear Science Symposium. Conference Record (IEEE Cat. No.03CH37515)*. Vol. 3. 2003, 1743–1745 Vol.3. DOI: 10.1109/NSSMIC.2003.1352215.

[26] International Standard ISO/IEC. *Programming Language C++*. 14882:2017(E). URL: https://isocpp.org/std/the-standard.

[27] Geant4 Collaboration. *Introduction to Geant4: Release 10.4*. URL: http://geant4-userdoc.web.cern.ch/geant4-userdoc/UsersGuides/IntroductionToGeant4/fo/BookIntroToGeant4.pdf.

[28] T Aso. *Scoring*. Toyama National College of Technology. Geant4 Tutorial at Seoul. 2011.

[29] Geant4 Collaboration. *Physics Reference Manual: Release 10.4*. URL: http://geant4-userdoc.web.cern.ch/geant4-userdoc/UsersGuides/IntroductionToGeant4/fo/BookIntroToGeant4.pdf.

[30] Geant4 Collaboration. *Geant4 User's Guide for Application Developers*. geant4 10.1. 2014.

[31] J. Seuntjies and D. W. O Rogers. "Monte Carlo Applications in Measurement Dosimetry". In: *Clinical Dosimetry Measurements in Radiotherapy (2009 AAPM Summer School)*. Ed. by D.W.O. Rogers and J.E Cygler. Medical Physics Publishing, 2009. Chap. 5, pp. 148–180.

[32] E. Reyes-Rivera et al. "Dosimetric study of surface applicators of HDR brachytherapy GammaMed Plus equipment". In: *AIP Conference Proceedings* 1626.1 (2014), pp. 181–184. DOI: 10.1063/1.4901388. eprint: https://aip.scitation.org/doi/pdf/10.1063/1.4901388. URL: https://aip.scitation.org/doi/abs/10.1063/1.4901388.

[33] D. C. Medich and J. J. Munro. "Monte Carlo characterization of the M-19 high dose rate Iridium-192 brachytherapy source". In: 34 (2007), pp. 1999–2006.

[34] JF López, J Donaire, and R Alcalde. "Monte Carlo dosimetry of the most commonly used ^{192}Ir high dose rate brachytherapy sources". In: *Rev Fis Med* 12(3) (2011), pp. 159–168.

[35] F. Salvat, J. M. Fernández-Varea, and J. Sempau. "PENELOPE-2008: A code system for Monte Carlo simulation of electron and photon transport". In: *Workshop Proceedings* (Barcelona, Spain), ISBN 978–92–64–99066–1.

[36] R. Abdullah et al. "High dose rate ^{192}Ir source calibration: A single institution experience". In: *Journal of Physics: Conf. Series* 851 (2017).

[37] L Chang et al. "Ir-192 Calibration in Air with Farmer Chamber for HDR Brachytherapy". In: *Journal of Medical and Biological Engineering* 36 (2016), pp. 145–152. DOI: 10.1007/s40846-016-0117-0.

[38] T. Sander. "Air kerma and absorbed dose standards for reference dosimetry in brachytherapy". In: *Br J Radiol* 87 (2014).

[39] R. King, S. Anderson, and M. Mills. "Geometry function of a linear brachytherapy source". In: *JOURNAL OF APPLIED CLINICAL MEDICAL PHYSICS (2)* 2 (2001), pp. 69–72.

[40] F. J. Reynoso, J. J. Munro III, and S.H. Cho. "Technical Note: Monte Carlo calculations of the AAPM TG-43 brachytherapy dosimetry parameters for a new titanium-encapsulated Yb-169 source". In: *J. Appl Clin Med Phys.* 18(4) (2017), pp. 193–199.

[41] F. Ballester et al. "Technical note: Monte-Carlo dosimetry of the HDR 12i and Plus ^{192}Ir sources". In: *Med. Phys. (12)* 28 (2001), pp. 2586–2591.

[42] The University of Florida Physics Department. *Statistical Analysis of Data: Exponential Decay and Poisson Processes*. URL: https://www.phys.ufl.edu/courses/phy4803L/group_I/gamma_spec/poisson.pdf.

[43] M. Palmer. *Statistical Analysis of Random Uncertainties*. URL: http://web.mit.edu/fluids-modules/www/exper_techniques/3.Statistical_Anal._of_Unce.pdf.

[44] F. Renner et al. “Uncertainties in Monte Carlo-based absorbed dose calculations for an experimental benchmark”. In: *Phys. Med. Biol.* 60 (2015), pp. 7637–7653.

[45] A.N. Viswanathan et al. “The American Brachytherapy Society Treatment Recommendations for Locally Advanced Carcinoma of the Cervix Part II: High Dose-Rate Brachytherapy”. In: *Brachytherapy* 11 (2012), pp. 47–52.

[46] A. Panchal and B. Tom. “Poster Viewing Abstract”. English. In: *International Journal of Radiation Oncology, Biology, Physics* 75(3 Supplement) (2009). doi:10.1016/j.ijrobp.2009.07.1641, S720–S721.

[47] X. S. Yang. “Harmony Search as a Metaheuristic Algorithm”. In: *Music-Inspired Harmony Search Algorithm. Studies in Computational Intelligence, Vol 191*. Ed. by Z. W. Geem. Springer, Berlin, Heidelberg, 2009.

[48] E.G. Schellenberg and S.E. Trehub. “Frequency ratios and the perception of tone patterns”. In: *Psychonomic Bulletin & Review* 1 (1994), pp. 191–201.

[49] A Holm. “Mathematical Optimization of HDR Brachytherapy”. PhD thesis. Department of Mathematics, Linkoping University, Sweden, 2013.

[50] R. Brun and F Rademakers. “ROOT - An Object Oriented Data Analysis Framework (Proceedings AIHENP’96 Workshop, Lausanne, Sep. 1996)”. In: *Nucl. Inst. & Meth. in Phys. Res. A* 389 (1997), pp. 81–86. URL: `http://root.cern.ch/`.

[51] K. Jabbari. “Review of Fast Monte Carlo Codes for Dose Calculation in Radiation Therapy Treatment Planning”. In: *Journal of Medical Signals and Sensors* 1(1) (2011), pp. 73–86.